

The University of Reading

Lagrange-Remap Methods for the Euler
Equations for Single and Multi Gas Flows

D.A. Bailey

3rd March 2003

Numerical Analysis Report 01/03

DEPARTMENT OF MATHEMATICS

Abstract

A solution method for the computation of steady Euler flows in one-dimension is presented. The approach is to combine the solution of the governing equations in a Lagrangian reference frame with an algorithm to remap the computational mesh. The aim is to retain the accuracy inherent with Lagrangian schemes and to avoid grid tangling and distortion scenarios.

The Lagrangian phase consists of a finite volume scheme which employs an approximate Riemann solver to evaluate intercell numerical fluxes. The HLLC and Roe Riemann solvers are considered. The Rezoning phase is simply an advection algorithm. Piecewise constant and piecewise linear advection schemes are investigated.

A technique is introduced to improve the resolution of the split scheme numerical solution profile at a material interface. The premiss is to allow a Lagrangian-type scheme at the interface to coexist with a split scheme for regions away from the interface. The methodology permits the existence of two non-uniform computational cells either side of the interface and suppresses the remap procedure at the interface. To prevent the creation of disproportionate non-uniform cells and interaction between the interface and a mesh boundary, the rezoning operation is augmented with a reconstruction algorithm.

The proposed two-step Lagrange-Remap or split methods are tested on Sod's shock tube problem and comparisons made between the Lagrange-Remap schemes and their Eulerian (unsplit) and pure Lagrangian counterparts.

The interface tracking method is tested on shock tube problems containing two different gases.

Acknowledgments

I would like to thank my supervisors Dr. P.K. Sweby and Dr. P. Glaister (University of Reading Mathematics Department) for their help and guidance with this work.

I would also like to acknowledge the financial support of AWE (Atomic Weapons Establishment) Aldermaston.

Contents

1	Introduction	3
2	Discretisation of the Governing Equations	4
3	The HLLC Solver	7
4	The Roe Solver	14
5	Rezoning	19
6	Interface Tracking	23
7	Numerical Results	31
8	Conclusions	36
9	Extensions	37

1 Introduction

The Euler equations for one-dimensional unsteady compressible flow, in the reference frame of a moving control volume, can be expressed in integral form as

$$\frac{\partial}{\partial t} \int_{\Omega(t)} \mathbf{U} \, d\Omega + \int_{\Gamma(t)} \hat{n} \cdot \mathbf{F} \, d\Gamma = 0. \quad (1)$$

$\Omega(t)$ is the moving control volume enclosed by its boundary $\Gamma(t)$, and \hat{n} denotes the outward normal to the boundary $\Gamma(t)$. The vector of conserved variables \mathbf{U} and the flux vector \mathbf{F} are given by

$$\mathbf{U} = \begin{pmatrix} \rho \\ \rho u \\ \rho E \end{pmatrix} \quad \text{and} \quad \mathbf{F} = \begin{pmatrix} (u - \dot{x})\rho \\ (u - \dot{x})\rho u + p \\ (u - \dot{x})\rho E + up \end{pmatrix}, \quad (2)$$

where ρ is the density, u is the fluid velocity, \dot{x} is the velocity of $\Gamma(t)$, E is the specific total energy, and p is the pressure. The system (1)-(2) represents conservation of mass, momentum and energy. When $\dot{x} = 0$, the system corresponds to the Eulerian description of conservation, whereas $\dot{x} = u$ results in the Lagrangian form, where the control volume moves with the instantaneous fluid velocity. The generality or arbitrariness of the description offered by equations (1)-(2) has rewarded them with the name Arbitrary Lagrangian-Eulerian (ALE) form of the conservation laws [5]. The set of equations is completed by the addition of an equation of state. The ideal gas equation of state is employed in this work and is given by

$$p = (\gamma - 1)\rho e, \quad (3)$$

where $e = E - \frac{1}{2}u^2$ is the specific internal energy and γ is a constant representing the ratio of specific heat capacities of the fluid.

This work focuses on solving the governing equations (1)-(2) in a Lagrangian reference frame. Therefore, it is assumed $\dot{x} = u$, and the vectors \mathbf{U} and \mathbf{F} take the form

$$\mathbf{U} = \begin{pmatrix} \rho \\ \rho u \\ \rho E \end{pmatrix} \quad \text{and} \quad \mathbf{F} = \begin{pmatrix} 0 \\ p \\ up \end{pmatrix}. \quad (4)$$

When formulating Lagrangian methods it is necessary to combine the schemes with an algorithm to rezone the computational mesh. This is because, as time advances, severe grid distortion or tangling may destroy the calculations. The

Lagrangian phase can then be considered as a solution for the sound wave related transport, and the rezoning of the grid can be viewed as the solution for the advection related transport [6].

The presentation of the proposed solution method is divided into eight sections. Section 2 is concerned with the discretisation of the governing equations. Sections 3 and 4 respectively derive the HLLC and the Roe Riemann solvers for the Euler equations in a Lagrangian frame of reference. Section 5 is devoted to algorithms for rezoning of the mesh. Material interface tracking is considered in Section 6. Numerical results are displayed and discussed in Section 7. Finally, conclusions and proposed extensions of the work can be found in Sections 8 and 9 respectively.

2 Discretisation of the Governing Equations

The spatial domain $[0, L]$ is discretised into M computational cells or finite volumes $I_i = [x_{i-\frac{1}{2}}, x_{i+\frac{1}{2}}]$ initially of uniform size $\Delta x_i = x_{i+\frac{1}{2}} - x_{i-\frac{1}{2}} = \Delta x = L/M$, with $i = 0, \dots, M-1$. For a given cell I_i the location of the cell centre or particle position is denoted by x_i . The value of the conserved variables for cell I_i , denoted by \mathbf{U}_i , are cell averaged values and are stored at the cell centre x_i . Therefore,

$$\mathbf{U}_i = \frac{1}{\Delta x_i} \int_{x_{i-\frac{1}{2}}}^{x_{i+\frac{1}{2}}} \mathbf{U}(x) dx \quad (5)$$

where $\mathbf{U}(x)$ is the data distribution. The temporal domain $[0, T]$, where T is some output time and not a boundary, is discretised into time steps Δt of variable size. A superscript is used to identify a particular time level. Figure (1) is an $x - t$ diagram of the computational mesh.

The governing equations (1) and (4) are discretised via the finite volume formula

$$\frac{\mathbf{U}_i^{n+1} \Omega_i^{n+1} - \mathbf{U}_i^n \Omega_i^n}{\Delta t} = - \left(\mathbf{F}_{i+\frac{1}{2}} - \mathbf{F}_{i-\frac{1}{2}} \right), \quad (6)$$

where Δt is the time step from time t^n to time t^{n+1} , Ω_i^n is the cell volume at time t^n , and $\mathbf{F}_{i-\frac{1}{2}}$ is the numerical flux across cell boundary $x_{i-\frac{1}{2}}$. From a practical point of view, and according to the explicit approach, equation (6) can be rewritten in the more convenient form

$$\mathbf{U}_i^{n+1} = \frac{\Omega_i^n}{\Omega_i^{n+1}} \left(\mathbf{U}_i^n + \frac{\Delta t}{\Omega_i^n} \left[\mathbf{F}_{i-\frac{1}{2}} - \mathbf{F}_{i+\frac{1}{2}} \right] \right). \quad (7)$$

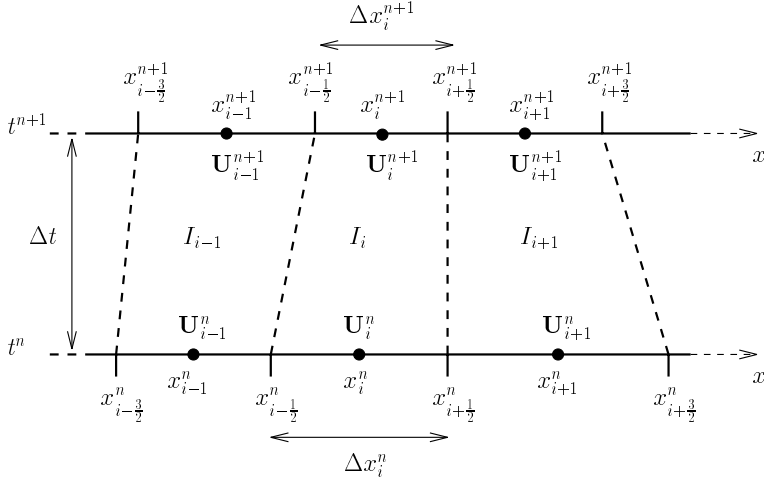


Figure 1: $x - t$ diagram of the computational mesh

In order to preserve conservation, the volume for cell I_i is updated by discretising the one-dimensional geometric conservation law (GCL)

$$\frac{\partial \Omega_i}{\partial t} - \int_{\Gamma_i(t)} \dot{x} \cdot \hat{n} \, d\Gamma = 0 \quad (8)$$

in the following manner

$$\frac{\Omega_i^{n+1} - \Omega_i^n}{\Delta t} = -\dot{x}_{i-\frac{1}{2}} + \dot{x}_{i+\frac{1}{2}}. \quad (9)$$

Here $\dot{x}_{i-\frac{1}{2}}$ is the grid velocity normal to the boundary $x_{i-\frac{1}{2}}$. Therefore, since $\dot{x} = u$ (Lagrangian reference frame), the volume is explicitly updated via

$$\Omega_i^{n+1} = \Omega_i^n - \Delta t \left(u_{i-\frac{1}{2}} - u_{i+\frac{1}{2}} \right). \quad (10)$$

where $u_{i-\frac{1}{2}}$ is the fluid velocity normal to the boundary $x_{i-\frac{1}{2}}$. Equivalently,

$$\Omega_i^{n+1} = \Omega_i^n - \left(x_{i-\frac{1}{2}}^{n+1} - x_{i+\frac{1}{2}}^{n+1} \right), \quad (11)$$

where $x_{i-\frac{1}{2}}^{n+1} = \Delta t u_{i-\frac{1}{2}}$ is the location of boundary $x_{i-\frac{1}{2}}$ at time t^{n+1} .

Time integration of particle position x_i is performed according to an estimate of the displacement of the centre of volume of cell I_i ,

$$x_i^{n+1} = \frac{1}{\Omega_i^n + \Delta\Omega_i} \left(x_i^n \Omega_i^n + \left(g_{i-\frac{1}{2}} z_{i-\frac{1}{2}} + g_{i+\frac{1}{2}} z_{i+\frac{1}{2}} \right) \right), \quad (12)$$

where $z_{i-\frac{1}{2}} = \hat{u}_{i-\frac{1}{2}} \Delta t$ is the additional cell volume created by normal displacement of the boundary $x_{i-\frac{1}{2}}^n$, ($\hat{u}_{i-\frac{1}{2}}$ is the outward normal velocity to the boundary $x_{i-\frac{1}{2}}^n$), $g_{i-\frac{1}{2}} = (x_{i-\frac{1}{2}}^n + u_{i-\frac{1}{2}} \Delta t / 2)$ is the position of the centre of $z_{i-\frac{1}{2}}$, and $\Delta\Omega_i = \sum_{j=0}^1 z_{i-\frac{1}{2}+j}$ is the total change in cell I_i volume over time interval Δt [1].

This calculation can be viewed as a weighted average of the positions of the centres of the individual volumes which make-up the cell volume at time t^{n+1} . The weights are equal to the value of the individual volumes.

In order to advance the flow solution at a particle using equation (7) the numerical flux vector is required on each of the boundaries of the cell. Each numerical flux is obtained by calculating an approximate solution to the Riemann problem that exists at the respective boundary. The two Riemann solvers used in this work are the HLLC and the Roe schemes. Both are described in detail in the following two sections.

Control of the time step size is achieved, prior to each time step, by selecting Δt such that none of the waves resulting from a Riemann problem at a cell boundary transverse more than half a cell width of the Eulerian mesh. The time step Δt from time level t^n to t^{n+1} is thus calculated using the formula

$$\Delta t = \frac{C_{cfl} \Delta x_i^0}{S_{\max}^n}, \quad (13)$$

where $C_{cfl} = 0.5$ and S_{\max}^n is an upper bound on the wave speeds present throughout the domain at time level n . There are various ways of estimating S_{\max}^n , and for the time-dependent, one-dimensional Euler equations a reliable choice is given by

$$S_{\max}^n = \max_i \{|u_i^n| + a_i^n\}, \quad i = 0, \dots, M, \quad (14)$$

where $a_i^n = \sqrt{\frac{\gamma p_i^n}{\rho_i^n}}$ is the local sound speed approximation [12].

However, equation (14) can lead to an underestimate of S_{\max}^n . For example, assume shock-tube data in which the flow is stationary at time t^0 .

Here $u_i^n = 0$ and the sound speed is the only contribution to S_{\max}^n . Underestimating the value of S_{\max}^n results in a choice of Δt that is too large and instabilities may develop from the beginning of the computations. To circumvent this problem the C_{cfl} constant in (13) is reduced to 0.1 for the first 5 time steps of the simulation.

3 The HLLC Solver

The HLLC scheme [13] is a modification of the HLL Riemann solver of Harten, Lax and van Leer [3]. In the HLL scheme the full Riemann problem is reduced to an approximate solution in which the wave configuration consists of two waves separating three constant states. The two waves represent the two non-linear discontinuities in the exact Riemann solution. In the HLLC solver, the missing contact wave is restored. Thus the approximate Riemann solution for the HLLC scheme consists of four constant states separated by three waves. Here, the essential features of HLLC are derived for the Lagrangian frame following the approach suggested by G.Ball [1].

Figure 2 is an $x - t$ diagram of the resulting wave structure for two adjacent cells I_i and I_{i+1} , on a Lagrangian one-dimensional grid, with piecewise constant data states $\mathbf{U}_L = \mathbf{U}_i^n$ and $\mathbf{U}_R = \mathbf{U}_{i+1}^n$

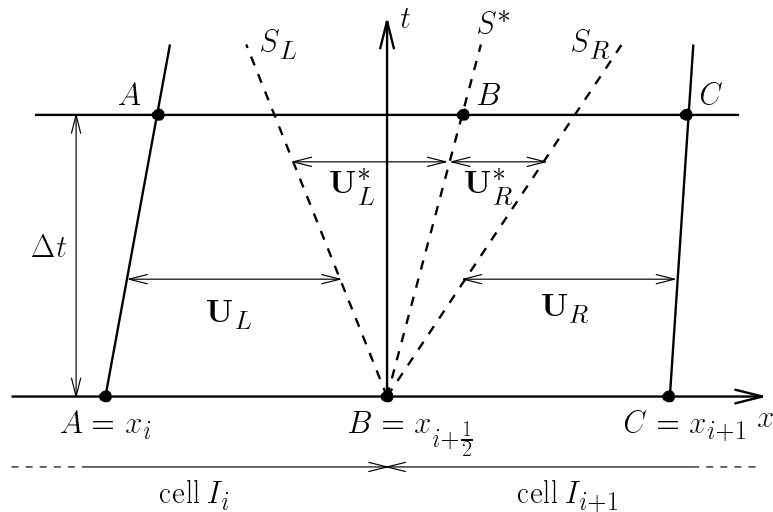


Figure 2: Schematic of approximate Riemann solution in Lagrangian control volume ABC.

The cell particles and their movements are indicated by the lines $A-A$ and $C-C$. The interface between the two relevant cells, which by definition is the contact wave of the Riemann problem, has position through time indicated by the line $B-B$. The $*$ superscript denotes the wave-processed states i.e the data states that are created due to the passage of three waves emerging from the origin of the initial discontinuity. S_L , S^* , and S_R are respectively the speed estimates for the left, contact and right waves.

It is required to calculate a numerical flux across the line $B-B$, that is across the cell interface, over time interval Δt .

Applying conservation of \mathbf{U} on $A-B$ over the time interval Δt gives

$$\left(\frac{\Delta x}{2} - u_L \Delta t + S_L \Delta t\right) \mathbf{U}_L + (-b_L \Delta t) + \Delta t S^* \mathbf{U}_L^* \quad (15)$$

$$= \frac{\Delta x}{2} \mathbf{U}_L + \Delta t \mathbf{F}_L - \Delta t \mathbf{F}_L^*$$

$$\Rightarrow (S_L - u_L) \mathbf{U}_L + (S^* - S_L) \mathbf{U}_L^* = \mathbf{F}_L - \mathbf{F}_L^* \quad (16)$$

$$\Rightarrow \mathbf{F}_L^* + (S^* - S_L) \mathbf{U}_L^* = \mathbf{F}_L + (u_L - S_L) \mathbf{U}_L \quad (17)$$

$$\Rightarrow \mathbf{F}_L^* = \mathbf{F}_L + \mathbf{U}_L^* (S^* - S_L) - \mathbf{U}_L (S_L - u_L) \quad (18)$$

Similarly, conservation of \mathbf{U} on $B-C$ over the time interval Δt yields

$$\mathbf{F}_R^* + (S^* - S_R) \mathbf{U}_R^* = \mathbf{F}_R + (u_R - S_R) \mathbf{U}_R \quad (19)$$

$$\Rightarrow \mathbf{F}_R^* = \mathbf{F}_R + \mathbf{U}_R^* (S^* - S_R) - \mathbf{U}_R (S_R - u_R) \quad (20)$$

The wave processed states and the corresponding lagrangian fluxes take the form

$$\mathbf{U}_K^* = \begin{pmatrix} \rho_K^* \\ \rho_K^* u_K^* \\ \rho_K^* E_K^* \end{pmatrix} \quad \text{and} \quad \mathbf{F}_K^* = \begin{pmatrix} 0 \\ p_K^* \\ u_K^* p_K^* \end{pmatrix}, \quad (21)$$

where $K = L, R$ and $S^* = u_L^* = u_R^* = u^* = u_{i+\frac{1}{2}}$ is an approximation of the fluid velocity normal to the boundary $x_{i+\frac{1}{2}}$. Therefore, by substitution of these quantities into (17) and (19), and by consideration of the individual rows of these vector equations, it can be shown that

$$\rho_K^* = \rho_K \frac{(S_K - u_K)}{(S_K - S^*)}, \quad (22)$$

$$\rho_K^* u_K^* = \rho_K \frac{(S_K - u_K)}{(S_K - S^*)} S^*, \quad (23)$$

$$p_K^* = p_K + \rho_K (u_K - S_K) (u_K - S^*), \quad (24)$$

and

$$\rho_K^* E_K^* = \rho_K \frac{(S_L - u_L)}{(S_L - S^*)} \left[E_K + (S^* - u_K) \left(S^* + \frac{p_K}{\rho_K (S_K - u_K)} \right) \right], \quad (25)$$

for $K = L, R$. The intercell numerical flux is then calculated via averaging of equations (18) and (20)

$$\mathbf{F}_{i+\frac{1}{2}} = (\mathbf{F}_L^* + \mathbf{F}_R^*) / 2, \quad (26)$$

where the \mathbf{U}_K^* , $K = L, R$, vector in (18) and (20) are obtained using equations (22), (23) and (25).

Following the original approach suggested by Toro et. al. [12], the wave speed estimates, S_L, S^* and S_R , are acquired from

$$S_L = u_L - a_L q_L, \quad S^* = u^*, \quad S_R = u_R + a_R q_R, \quad (27)$$

where a_L, a_R are the local sound speeds in the undisturbed fluid, and q_K , for $K = L, R$, is a parameter defined by

$$q_K = \begin{cases} 1 & H_K \leq 1 \\ \sqrt{1 + \frac{\gamma+1}{2\gamma} (H_K - 1)} & \text{otherwise} \end{cases}. \quad (28)$$

Here $H_K = \tilde{p}^*/p_K$, and \tilde{p}^* and u^* are estimates for the wave processed pressure and velocity. If the K wave is a rarefaction then the speed S_K corresponds to the characteristic speed of the head of the rarefaction. If the wave is a shock then S_K corresponds to an approximation to the true shock speed; the wave relations used are exact but the pressure ratio across the discontinuity is approximated, because the value of \tilde{p}^* is an estimate.

In this work, values for \tilde{p}^* and u^* are calculated using the adaptive/hybrid approach proposed by Toro [12], which is based on his exact Riemann solver. The method is described algorithmically below:

- The initial approximation for the pressure is evaluated using

$$\tilde{p}_{\text{int}}^* = \frac{1}{2} (p_L + p_R) - \frac{1}{2} (u_L - u_R) \bar{\rho} \bar{a}, \quad (29)$$

where $\bar{a} = (a_L + a_R) / 2$ and $\bar{\rho} = (\rho_L + \rho_R) / 2$.

- If $\tilde{p}_{\text{int}}^* > p_{\min}$ and $\tilde{p}_{\text{int}}^* < p_{\max}$, and $Q = p_{\max} / p_{\min} < 2$, where $p_{\min} = \min(p_L, p_R)$ and $p_{\max} = \max(p_L, p_R)$, then

$$\tilde{p}^* = \max(\text{tolerance}, \tilde{p}_{\text{int}}^*), \quad (30)$$

$$u^* = \frac{(u_L + u_R)}{2} - \frac{(p_R - p_L)}{2\bar{a}\bar{\rho}}. \quad (31)$$

- If $\tilde{p}_{\text{int}}^* < p_{\text{min}}$, suggesting that the 2 non-linear waves in the exact solution to the Riemann problem are rarefaction waves, then

$$\tilde{p}^* = \left[\frac{a_L + a_R - \frac{\gamma-1}{2}(u_R - u_L)}{\frac{a_L}{p_L^z} + \frac{a_R}{p_R^z}} \right]^{\frac{1}{z}}, \quad (32)$$

$$u^* = u_L - \frac{2a_L}{(\gamma-1)} \left[\left(\frac{\tilde{p}^*}{p_L} \right)^z - 1 \right]. \quad (33)$$

where $z = \frac{\gamma-1}{2\gamma}$.

- Else the 2 non-linear waves in the exact solution of the Riemann problem are assumed to be shock waves, and

$$\tilde{p}^* = \frac{g_L(p_0)p_L + g_R(p_0)p_R - (u_R - u_L)}{g_L(p_0) + g_R(p_0)}, \quad (34)$$

$$u^* = \frac{1}{2}(u_L + u_R) + \frac{1}{2}[(\tilde{p}^* - p_R)g_R(p_0) - (\tilde{p}^* - p_L)g_L(p_0)], \quad (35)$$

where

$$g_K(p) = \left[\frac{A_K}{p + B_K} \right]^{\frac{1}{2}}, \quad (36)$$

$$A_K = \frac{2}{(\gamma+1)\rho_K}, \quad (37)$$

$$B_K = \frac{(\gamma-1)}{(\gamma+1)}p_K, \quad K = L, R, \quad (38)$$

and

$$p_0 = \max(0, \tilde{p}_{\text{int}}^*). \quad (39)$$

The initial approximation for the pressure (29), and the velocity approximation (31), were achieved by writing the governing equations in terms of the primitive variables $\mathbf{W} = (\rho, u, p)$, linearising about the constant state $\overline{\mathbf{W}} = \frac{1}{2}(\mathbf{W}_L + \mathbf{W}_R)$, and then applying the Rankine-Hugoniot jump conditions across left and right waves. The condition $Q < 2$ ensures that the pressure data values p_L and p_R are not widely different. Equations (32) to (39) were derived by assuming the appropriate wave structure and applying exact wave relations across the discontinuities. The 2-shock equations require the use of the initial pressure estimation (29) since the approach does not lead to a close form solution.

Second Order Accuracy For HLLC

In this work, second order accuracy for the Lagrangian HLLC Riemann solver is achieved using the MUSCL-Hancock approach [12]. The method can be divided into 3 stages:

Stage 1: Data Reconstruction

The piecewise constant data cell average values \mathbf{U}_i^n are locally replaced by piecewise linear functions in each cell $[x_{i-\frac{1}{2}}, x_{i+\frac{1}{2}}]$ according to

$$\mathbf{U}_i^n(x) = \mathbf{U}_i^n + (x - x_i)\tilde{\sigma}_i, \quad x \in [x_{i-\frac{1}{2}}, x_{i+\frac{1}{2}}], \quad (40)$$

where $\tilde{\sigma}_i$ is a vector of limited first derivative approximations. The values of $\mathbf{U}_i^n(x)$ at the cell boundaries of cell I_i are

$$\mathbf{U}_i^L = \mathbf{U}_i^n - \frac{\Delta x_i}{2}\tilde{\sigma}_i \quad \text{and} \quad (41)$$

$$\mathbf{U}_i^R = \mathbf{U}_i^n + \frac{\Delta x_i}{2}\tilde{\sigma}_i, \quad (42)$$

and are called boundary extrapolated values.

The two alternative methods used in this work for evaluating the vector $\tilde{\sigma}_i$ are described in detail in the next subsection.

Stage 2: Evolution

The boundary extrapolated values \mathbf{U}_i^L and \mathbf{U}_i^R are considered to be cell average values, and are evolved by $\frac{1}{2}\Delta t$ using a conservative scheme in which the numerical flux is equal to the exact flux function evaluated at the extrapolated values. That is,

$$\overline{\mathbf{U}}_i^L = \mathbf{U}_i^L + \frac{1}{2} \frac{\Delta t}{\Delta x_i^n} [\mathbf{F}(\mathbf{U}_i^L) - \mathbf{F}(\mathbf{U}_i^R)], \quad (43)$$

$$\overline{\mathbf{U}}_i^R = \mathbf{U}_i^R + \frac{1}{2} \frac{\Delta t}{\Delta x_i^n} [\mathbf{F}(\mathbf{U}_i^L) - \mathbf{F}(\mathbf{U}_i^R)]. \quad (44)$$

Stage 3: The Riemann Problem

To calculate the intercell flux one now solves the Riemann problem with data

$$\mathbf{U}_L \equiv \overline{\mathbf{U}}_i^R \quad ; \quad \mathbf{U}_R \equiv \overline{\mathbf{U}}_i^L. \quad (45)$$

The generalised Riemann problem created by the piecewise linear data (40) is ignored.

Evaluating the vector $\tilde{\sigma}_i$.

Two methods are considered for evaluating the vector of limited first derivative approximations, namely conserved variable slope limiting and wave-by-wave slope limiting.

Conserved Variable Slope Limiting.

The vector $\tilde{\sigma}_i$ in cell I_i is taken to be a function of the derivatives $\left(\frac{\Delta_{i-\frac{1}{2}}}{\Delta x_{i-\frac{1}{2}}}\right)$ and $\left(\frac{\Delta_{i+\frac{1}{2}}}{\Delta x_{i+\frac{1}{2}}}\right)$, namely

$$\tilde{\sigma}_i = \tilde{\sigma}_i \left(\frac{\Delta_{i-\frac{1}{2}}}{\Delta x_{i-\frac{1}{2}}}, \frac{\Delta_{i+\frac{1}{2}}}{\Delta x_{i+\frac{1}{2}}} \right), \quad (46)$$

where

$$\Delta_{i-\frac{1}{2}} = \mathbf{U}_i^n - \mathbf{U}_{i-1}^n \quad ; \quad \Delta_{i+\frac{1}{2}} = \mathbf{U}_{i+1}^n - \mathbf{U}_i^n; \quad (47)$$

$$\Delta x_{i-\frac{1}{2}} = x_i - x_{i-1} \quad ; \quad \Delta x_{i+\frac{1}{2}} = x_{i+1} - x_i. \quad (48)$$

The limited derivatives are evaluated component-wise using

$$\begin{aligned} & \tilde{\sigma}_i \left(\frac{\Delta_{i-\frac{1}{2}}}{\Delta x_{i-\frac{1}{2}}}, \frac{\Delta_{i+\frac{1}{2}}}{\Delta x_{i+\frac{1}{2}}} \right) \\ &= \begin{cases} \max \left[0, \min \left(\frac{\beta \Delta_{i-\frac{1}{2}}}{\Delta x_{i-\frac{1}{2}}}, \frac{\Delta_{i+\frac{1}{2}}}{\Delta x_{i+\frac{1}{2}}} \right), \min \left(\frac{\Delta_{i-\frac{1}{2}}}{\Delta x_{i-\frac{1}{2}}}, \frac{\beta \Delta_{i+\frac{1}{2}}}{\Delta x_{i+\frac{1}{2}}} \right) \right] & \Delta_{i+\frac{1}{2}} \geq 0 \\ \min \left[0, \max \left(\frac{\beta \Delta_{i-\frac{1}{2}}}{\Delta x_{i-\frac{1}{2}}}, \frac{\Delta_{i+\frac{1}{2}}}{\Delta x_{i+\frac{1}{2}}} \right), \max \left(\frac{\Delta_{i-\frac{1}{2}}}{\Delta x_{i-\frac{1}{2}}}, \frac{\beta \Delta_{i+\frac{1}{2}}}{\Delta x_{i+\frac{1}{2}}} \right) \right] & \Delta_{i+\frac{1}{2}} \leq 0 \end{cases} \end{aligned} \quad (49)$$

where the value $\beta = 1$ reproduces a minmod-type limiter, and $\beta = 2$ reproduces a superbee-type limiter.

Equation (49) has been established by forcing equivalence of MUSCL-type schemes with conventional flux limiter methods, for the model scalar equation on a fixed Eulerian grid [12]. The result then being modified to allow for the varying cell volumes associated with Lagrangian methods.

Wave-By-Wave Slope Limiting.

The vector $\tilde{\sigma}_i$ in cell I_i is taken to be a function of the derivatives $\left(\frac{\Delta_{i-\frac{1}{2}}}{\Delta x_{i-\frac{1}{2}}}\right)$ and $\left(\frac{\Delta_{i+\frac{1}{2}}}{\Delta x_{i+\frac{1}{2}}}\right)$, namely

$$\tilde{\sigma}_i = \tilde{\sigma}_i \left(\frac{\Delta_{i-\frac{1}{2}}}{\Delta x_{i-\frac{1}{2}}}, \frac{\Delta_{i+\frac{1}{2}}}{\Delta x_{i+\frac{1}{2}}} \right), \quad (50)$$

where

$$\Delta_{i-\frac{1}{2}} = \mathbf{U}_i^n - \mathbf{U}_{i-1}^n \quad ; \quad \Delta_{i+\frac{1}{2}} = \mathbf{U}_{i+1}^n - \mathbf{U}_i^n; \quad (51)$$

$$\Delta x_{i-\frac{1}{2}} = x_i - x_{i-1} \quad ; \quad \Delta x_{i+\frac{1}{2}} = x_{i+1} - x_i. \quad (52)$$

The arguments $\Delta_{i-\frac{1}{2}}$ and $\Delta_{i+\frac{1}{2}}$ are then decomposed into jumps across waves emerging from the Riemann problems with data states $(\mathbf{U}_{i-1}^n, \mathbf{U}_i^n)$ and $(\mathbf{U}_i^n, \mathbf{U}_{i+1}^n)$;

$$\Delta_{i-\frac{1}{2}} = \sum_{m=1}^3 \Delta_{i-\frac{1}{2}}^{(m)} \quad ; \quad \Delta_{i+\frac{1}{2}} = \sum_{m=1}^3 \Delta_{i+\frac{1}{2}}^{(m)}, \quad (53)$$

where $\Delta_{i-\frac{1}{2}}^{(m)}$ is the jump across wave m at the interface $x_{i+\frac{1}{2}}$.

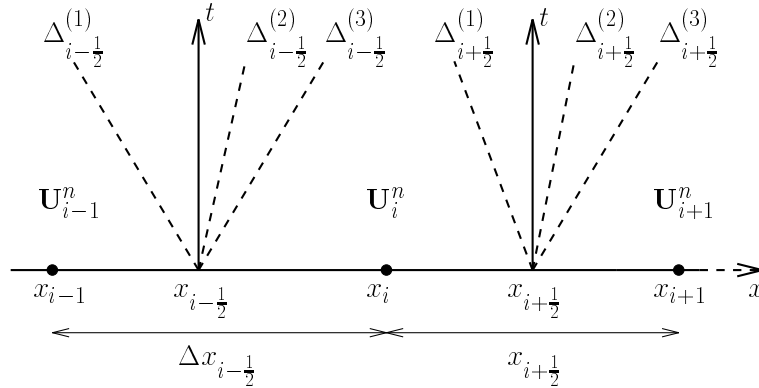


Figure 3: Wave-by-wave decomposition of gradients obtained from local solutions of Riemann problems, with cell averages as initial data.

Equation (50) can then be written as

$$\tilde{\sigma}_i = \sum_{m=1}^3 \tilde{\sigma}_i^{(m)} \left(\frac{\Delta_{i-\frac{1}{2}}^{(m)}}{\Delta x_{i-\frac{1}{2}}}, \frac{\Delta_{i+\frac{1}{2}}^{(m)}}{\Delta x_{i+\frac{1}{2}}} \right), \quad (54)$$

thus, allowing the limiting process to be applied wave-by-wave.

The limited derivatives are evaluated component-wise using

$$\begin{aligned} & \tilde{\sigma}_i^{(m)} \left(\frac{\Delta_{i-\frac{1}{2}}^{(m)}}{\Delta x_{i-\frac{1}{2}}}, \frac{\Delta_{i+\frac{1}{2}}^{(m)}}{\Delta x_{i+\frac{1}{2}}} \right) \\ &= \begin{cases} \max \left[0, \min \left(\frac{\beta \Delta_{i-\frac{1}{2}}^{(m)}}{\Delta x_{i-\frac{1}{2}}}, \frac{\Delta_{i+\frac{1}{2}}^{(m)}}{\Delta x_{i+\frac{1}{2}}} \right), \min \left(\frac{\Delta_{i-\frac{1}{2}}^{(m)}}{\Delta x_{i-\frac{1}{2}}}, \frac{\beta \Delta_{i+\frac{1}{2}}^{(m)}}{\Delta x_{i+\frac{1}{2}}} \right) \right] & \Delta_{i+\frac{1}{2}}^{(m)} \geq 0 \\ \min \left[0, \max \left(\frac{\beta \Delta_{i-\frac{1}{2}}^{(m)}}{\Delta x_{i-\frac{1}{2}}}, \frac{\Delta_{i+\frac{1}{2}}^{(m)}}{\Delta x_{i+\frac{1}{2}}} \right), \max \left(\frac{\Delta_{i-\frac{1}{2}}^{(m)}}{\Delta x_{i-\frac{1}{2}}}, \frac{\beta \Delta_{i+\frac{1}{2}}^{(m)}}{\Delta x_{i+\frac{1}{2}}} \right) \right] & \Delta_{i+\frac{1}{2}}^{(m)} \leq 0 \end{cases} \end{aligned} \quad (55)$$

where the value $\beta = 1$ reproduces a minmod-type limiter, and $\beta = 2$ reproduces a superbee-type limiter.

Equation (55) has been established by forcing equivalence of MUSCL-type schemes with conventional flux limiter methods, for the model scalar equation on a fixed Eulerian grid [12]. The result then being modified to allow for the varying cell volumes associated with Lagrangian methods.

4 The Roe Solver

The Roe solver calculates a numerical approximation to the solution of hyperbolic conservation laws by solving a constant coefficient linear system. That is, a modified conservation law is computed and solved to render a numerical approximation to the original problem [7]. Here, an adjustment to the fixed grid Roe scheme is derived to adapted the scheme to a Lagrangian reference frame [11]. The adjustment is designed to take into account mesh movement.

Figure 4 is an $x - t$ diagram of the resulting wave structure of the Roe approximation for two adjacent cells I_i and I_{i+1} , on a Lagrangian one-dimensional grid, with piecewise constant states $\mathbf{U}_L = \mathbf{U}_i^n$ and $\mathbf{U}_R = \mathbf{U}_{i+1}^n$.

The cell particles and their movements are indicated by the lines $A - A$ and $C - C$. The interface between the two relevant cells has position through time indicated by the line $B - B$. The $*$ superscript denotes the wave-processed states. The eigenvalues $\tilde{u} - \tilde{a}$, \tilde{u} , $\tilde{u} + \tilde{a}$ of the Roe Jacobian matrix $\tilde{A}(\mathbf{U}_L, \mathbf{U}_R)$ are, respectively, the wave speed estimates for the left, contact and right waves.

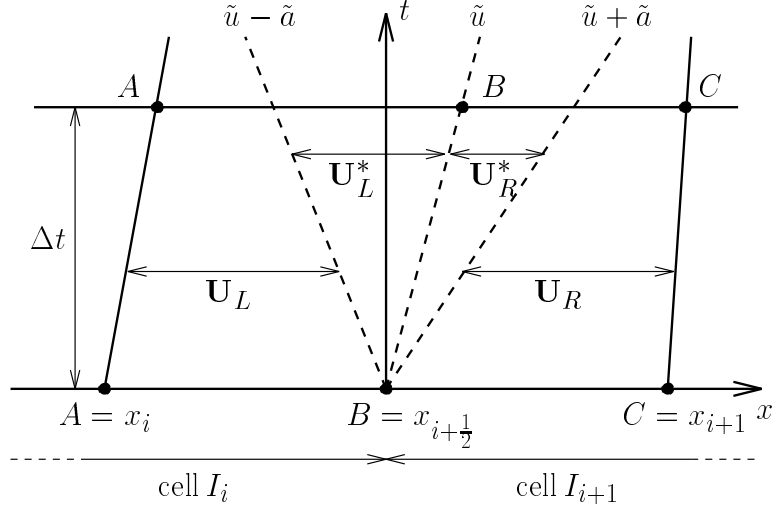


Figure 4: Schematic of approximate Riemann solution in Lagrangian control volume ABC.

For a fixed grid, diagonalising the Roe linearisation for the system of non-linear equations allows the flux between the two adjacent cells I_i and I_{i+1} (i.e the flux across the t -axis) to be written as

$$\mathbf{F}_{i+\frac{1}{2}}(\mathbf{U}_L, \mathbf{U}_R) = \frac{1}{2} \left[\mathbf{F}_L(\mathbf{U}_L) + \mathbf{F}_R(\mathbf{U}_R) - \sum_{m=1}^3 \tilde{\alpha}_{i+\frac{1}{2}}^{(m)} |\tilde{\lambda}_{\text{adv}}^{(m)} + \tilde{\lambda}_{\text{rel}}^{(m)}| \tilde{\mathbf{e}}_{i+\frac{1}{2}}^{(m)} \right], \quad (56)$$

where

$$\mathbf{F}_K(\mathbf{U}_K) = u_K \mathbf{U}_K + \begin{pmatrix} 0 \\ p_K \\ u_K p_K \end{pmatrix}, \quad K = L, R, \quad (57)$$

the wave strengths are given by

$$\tilde{\alpha}_{i+\frac{1}{2}}^{(1)} = \frac{1}{2\tilde{a}} [(\rho_R - \rho_L)(\tilde{u} + \tilde{a}) - (\rho_R u_R - \rho_L u_L) - \tilde{a} \tilde{\alpha}^{(2)}], \quad (58)$$

$$\tilde{\alpha}_{i+\frac{1}{2}}^{(2)} = \frac{\gamma - 1}{\tilde{a}^2} \left[(\rho_R - \rho_L) (\tilde{H} - \tilde{u}^2) + \tilde{u} (\rho_R u_R - \rho_L u_L) - (\rho_R E_R - \rho_L E_L) \right], \quad (59)$$

$$\tilde{\alpha}_{i+\frac{1}{2}}^{(3)} = (\rho_R - \rho_L) - (\tilde{\alpha}^{(1)} + \tilde{\alpha}^{(2)}), \quad (60)$$

the eigenvalues are

$$\tilde{\lambda}_{\text{adv}}^{(1)} = \tilde{u} \quad , \quad \tilde{\lambda}_{\text{rel}}^{(1)} = -\tilde{a} \quad , \quad (61)$$

$$\tilde{\lambda}_{\text{adv}}^{(2)} = \tilde{u} \quad , \quad \tilde{\lambda}_{\text{rel}}^{(2)} = 0 \quad , \quad (62)$$

$$\tilde{\lambda}_{\text{adv}}^{(3)} = \tilde{u} \quad , \quad \tilde{\lambda}_{\text{rel}}^{(3)} = \tilde{a} \quad , \quad (63)$$

and the corresponding right eigenvectors are

$$\tilde{\mathbf{e}}_{i+\frac{1}{2}}^{(1)} = \begin{pmatrix} 1 \\ \tilde{u} - \tilde{a} \\ \tilde{H} - \tilde{u}\tilde{a} \end{pmatrix}, \quad \tilde{\mathbf{e}}_{i+\frac{1}{2}}^{(2)} = \begin{pmatrix} 1 \\ \tilde{u} \\ \frac{1}{2}\tilde{u}^2 \end{pmatrix}, \quad \tilde{\mathbf{e}}_{i+\frac{1}{2}}^{(3)} = \begin{pmatrix} 1 \\ \tilde{u} + \tilde{a} \\ \tilde{H} + \tilde{u}\tilde{a} \end{pmatrix}. \quad (64)$$

Here, $\tilde{u} = u_{i+\frac{1}{2}}$ is an approximation of the fluid velocity normal to the boundary $x_{i+\frac{1}{2}}$, and

$$\tilde{u} = \frac{\sqrt{\rho_L}u_L + \sqrt{\rho_R}u_R}{\sqrt{\rho_L} + \sqrt{\rho_R}} \quad (65)$$

$$\tilde{H} = \frac{\sqrt{\rho_L}H_L + \sqrt{\rho_R}H_R}{\sqrt{\rho_L} + \sqrt{\rho_R}} \quad (66)$$

$$\tilde{a}^2 = (\gamma - 1) \left[\tilde{H} - \frac{1}{2}\tilde{u}^2 \right]. \quad (67)$$

Here H_K , $K = L, R$, is the total enthalpy

$$H_K = \frac{E_K + p_K}{\rho_K} \quad K = L, R. \quad (68)$$

The tilde is used to indicate a Roe averaged value.

The flux function (56) has been written in such a way that its value, the flux relative to a fixed grid, can be split naturally into two quantities; the flux which is a result of advection with the flow; and the flux relative to the flow.

Therefore, to determine the flux between the two cells I_i and I_{i+1} in a Lagrangian frame of reference (i.e. the flux across the $B - B$ in Figure 4), one simply subtracts the flux resulting from advection with the flow from equation (56)

$$\mathbf{F}_{i+\frac{1}{2}}(\mathbf{U}_L, \mathbf{U}_R) = \frac{1}{2} \left[\mathbf{F}_L(\mathbf{U}_L) + \mathbf{F}_R(\mathbf{U}_R) - \sum_{m=1}^3 \tilde{\alpha}_{i+\frac{1}{2}}^{(m)} |\tilde{\lambda}_{\text{rel}}^{(m)}| \tilde{\mathbf{e}}_{i+\frac{1}{2}}^{(m)} \right] \quad (69)$$

where

$$\mathbf{F}_K(\mathbf{U}_K) = \begin{pmatrix} 0 \\ p_K \\ u_K p_K \end{pmatrix}, \quad K = L, R, \quad (70)$$

and the remaining variables are given by equations (58) to (67).

It is well known that Roe's scheme for the Euler equations on a fixed grid permits non-physical stationary discontinuities; a sonic expansion wave may be incorrectly approximated by a rarefaction shock. Hence, Roe's approximate Riemann Solver in general does not satisfy an entropy inequality. However, it can be modified to eliminate these entropy violating discontinuities while retaining those that satisfy the entropy law. Such an entropy fix is not necessary in the Lagrangian case, because shock and expansion waves move with respect to the Lagrangian reference frame [15].

Second-Order Accuracy For Roe

In this work, second-order accuracy for the Lagrangian Roe solver is achieved using flux limiting. The method is to linearize the system of non-linear equations using Roe's approximate Riemann solver, diagonalise, and then apply flux-limiting to each of the resulting scalar equations [4].

Taking Godunov's scheme to calculate the first-order flux and the Lax-Wendroff scheme to evaluate the second-order flux, the numerical flux between cell I_i and I_{i+1} , for the corresponding fixed grid flux-limiter solver, can be written as

$$\mathbf{F}_{i+\frac{1}{2}}(\mathbf{U}_L, \mathbf{U}_R) = \frac{1}{2} \left[\mathbf{F}_L(\mathbf{U}_L) + \mathbf{F}_R(\mathbf{U}_R) - \sum_{m=1}^3 \left\{ \left[1 - \phi \cdot \left(1 - \frac{\Delta t}{\Delta x_{i+\frac{1}{2}}} |\tilde{\lambda}_{\text{adv}}^{(m)} + \tilde{\lambda}_{\text{rel}}^{(m)}| \right) \right] \cdot |\tilde{\lambda}_{\text{adv}}^{(m)} + \tilde{\lambda}_{\text{rel}}^{(m)}| \tilde{\alpha}_{i+\frac{1}{2}}^{(m)} \tilde{\mathbf{e}}_{i+\frac{1}{2}}^{(m)} \right\} \right]. \quad (71)$$

Here, the fluxes $\mathbf{F}_L, \mathbf{F}_R$, the wave strengths $\left(\tilde{\alpha}_{i+\frac{1}{2}}^{(m)}\right)$, the eigenvalues $\left(\tilde{\lambda}_{\text{adv}}^{(m)}, \tilde{\lambda}_{\text{rel}}^{(m)}\right)$ and the corresponding right eigenvectors $\left(\tilde{\mathbf{e}}_{i+\frac{1}{2}}^{(m)}\right)$ are given by equations (58) to (67). $\phi = \phi(r)$, where

$$r = \frac{\tilde{\alpha}_{i'}^{(m)}}{\tilde{\alpha}_{i+\frac{1}{2}}^{(m)}} \quad \text{and} \quad i' = i + \frac{1}{2} + \text{sign} \left(\tilde{\lambda}_{\text{adv}}^{(m)} + \tilde{\lambda}_{\text{rel}}^{(m)} \right) \quad (72)$$

is the limiter function. Three limiter functions are considered [12], namely

- the minbee limiter:

$$\phi(r) = \begin{cases} 0 & r \leq 0 \\ r & 0 \leq r \leq 1 \\ 1 & r \geq 1 \end{cases}, \quad (73)$$

- the van Leer limiter:

$$\phi(r) = \begin{cases} 0 & r \leq 0 \\ \frac{2r}{1+r} & r \geq 0 \end{cases}, \quad (74)$$

- the superbee limiter:

$$\phi(r) = \begin{cases} 0 & r \leq 0 \\ 2r & 0 \leq r \leq \frac{1}{2} \\ 1 & \frac{1}{2} \geq r \\ r & 1 \leq r \leq 2 \\ 2 & r \geq 2 \end{cases}. \quad (75)$$

Subtraction of the flux resulting from advection with the flow from equation (71) produces the required second-order accurate Lagrangian flux

$$\begin{aligned} \mathbf{F}_{i+\frac{1}{2}}(\mathbf{U}_L, \mathbf{U}_R) &= \frac{1}{2} \left[\mathbf{F}_L(\mathbf{U}_L) + \mathbf{F}_R(\mathbf{U}_R) - \right. \\ &\quad \left. \sum_{m=1}^3 \left\{ \left[1 - \phi \cdot \left(1 - \frac{\Delta t}{\Delta x_{i+\frac{1}{2}}} |\tilde{\lambda}_{\text{rel}}^{(m)}| \right) \right] \right. \right. \\ &\quad \left. \left. \cdot |\tilde{\lambda}_{\text{rel}}^{(m)}| \tilde{\alpha}_{i+\frac{1}{2}}^{(m)} \tilde{\mathbf{e}}_{i+\frac{1}{2}}^{(m)} \right\} \right], \quad (76) \end{aligned}$$

where $\mathbf{F}_L, \mathbf{F}_R$ are given by equation (70), $\phi = \phi(r)$ with

$$r = \frac{\tilde{\alpha}_{i'}^{(m)}}{\tilde{\alpha}_{i+\frac{1}{2}}^{(m)}} \quad \text{and} \quad i' = i + \frac{1}{2} + \text{sign} \left(\tilde{\lambda}_{\text{rel}}^{(m)} \right), \quad (77)$$

and the remaining variables are given by equations (58) to (67) and (73) to (75).

5 Rezoning

As time advances, solutions calculated using a Lagrangian scheme may become less accurate or even destroyed due to mesh distortion or tangling. To circumvent this failure the Lagrangian scheme can be combined with an algorithm to rezone or remap the grid. In this work the rezoning is carried out at each time step and the mesh is remapped back to the grid that was generated at the initial time level.

Rezoning involves fixing the fluid and then moving the mesh through the medium to return it to where it initially resided at the start of the Lagrangian phase. This process can be viewed as advecting the fluid through the mesh in pseudo time until, relative to the fluid, the mesh has been moved back to where it began.

The actual quantities remapped are the conserved variables of mass, momentum and internal energy (ρe). It is possible to remap total energy ($\rho (e + \frac{1}{2}u^2)$) and arguably this has improved energy conservation properties. However, if in the problem being considered virtually all of the energy is kinetic energy, then subtracting this from total energy to calculate rezoned internal energy, could, due to numerical inaccuracies, result in a physically incorrect negative value [10].

Mesh movement within the Lagrangian phase can result in a cell's position and volume being altered. Figures (5) and (6) contain $x-U$ diagrams of four possible outcomes of the Lagrangian phase for cell I_i . Diagrams (a) and (b) show, in turn, non-uniform movement to the left and to the right. Diagrams (c) and (d) respectively illustrate cell contraction and expansion.

The distance traveled by the boundary $x_{i-\frac{1}{2}}$ during the Lagrangian phase is denoted by $\delta\Omega_{i-\frac{1}{2}}$ and is calculated using the formula

$$\begin{aligned}\delta\Omega_{i-\frac{1}{2}} &= x_{i-\frac{1}{2}}^{n+1} - x_{i-\frac{1}{2}}^n \\ &= \Delta t \dot{x}_{i-\frac{1}{2}},\end{aligned}\tag{78}$$

where Δt is the time increment for the Lagrangian phase, and $\dot{x}_{i-\frac{1}{2}}$ ($= u_{i-\frac{1}{2}}$) is the grid (fluid) velocity normal to the boundary $x_{i-\frac{1}{2}}$. ($u_{i-\frac{1}{2}}$ is determined by the chosen Riemann solver).

Cell boundaries and centers are remapped by simply returning them to the position they held at the previous time level

$$\bar{x}_{i-\frac{1}{2}} = x_{i-\frac{1}{2}}^n,\tag{79}$$

$$\bar{x}_i = x_i^n.\tag{80}$$

The overbar is used to indicate post-remap values.

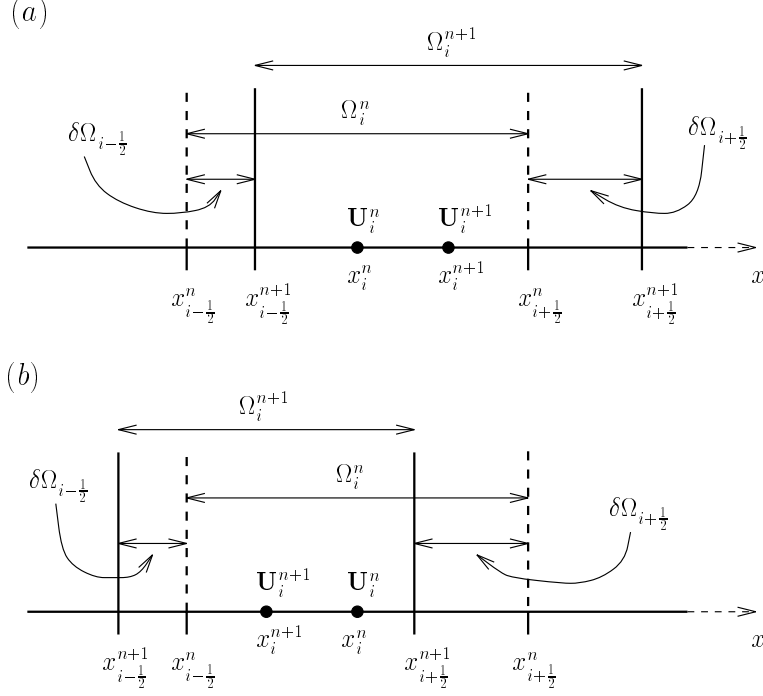


Figure 5: $x - U$ diagrams for cell I_i of non-uniform movement to the left and to the right resulting from the Lagrangian phase.

Re-initialisation of \mathbf{U}_i , required due to the rezoning of cell I_i from $[x_{i-\frac{1}{2}}^{n+1}, x_{i+\frac{1}{2}}^{n+1}]$ to $[\bar{x}_{i-\frac{1}{2}}, \bar{x}_{i+\frac{1}{2}}] = [x_{i-\frac{1}{2}}^n, x_{i+\frac{1}{2}}^n]$, is performed using the conservative finite volume formula

$$\bar{\mathbf{U}}_i = \frac{1}{\bar{\Omega}_i} \left(\Omega_i^{n+1} \mathbf{U}_i^{n+1} + \delta\Omega_{i-\frac{1}{2}} \hat{\mathbf{F}}_{i-\frac{1}{2}} - \delta\Omega_{i+\frac{1}{2}} \hat{\mathbf{F}}_{i+\frac{1}{2}} \right), \quad (81)$$

where

$$\mathbf{U} = \begin{pmatrix} \rho \\ \rho u \\ \rho e \end{pmatrix}, \quad (82)$$

Ω_i^{n+1} is the volume of cell I_i as a result of the Lagrange phase, $\delta\Omega_{i-\frac{1}{2}}$ is given by equation (78), and $\hat{\mathbf{F}}_{i-\frac{1}{2}}$ is a vector of conserved variable averages for the interval $[x_{i-\frac{1}{2}}^n, x_{i+\frac{1}{2}}^n]$. The components of $\hat{\mathbf{F}}_{i-\frac{1}{2}}$ correspond component-wise to the conserved variables in the vector \mathbf{U} . Their values are determined by

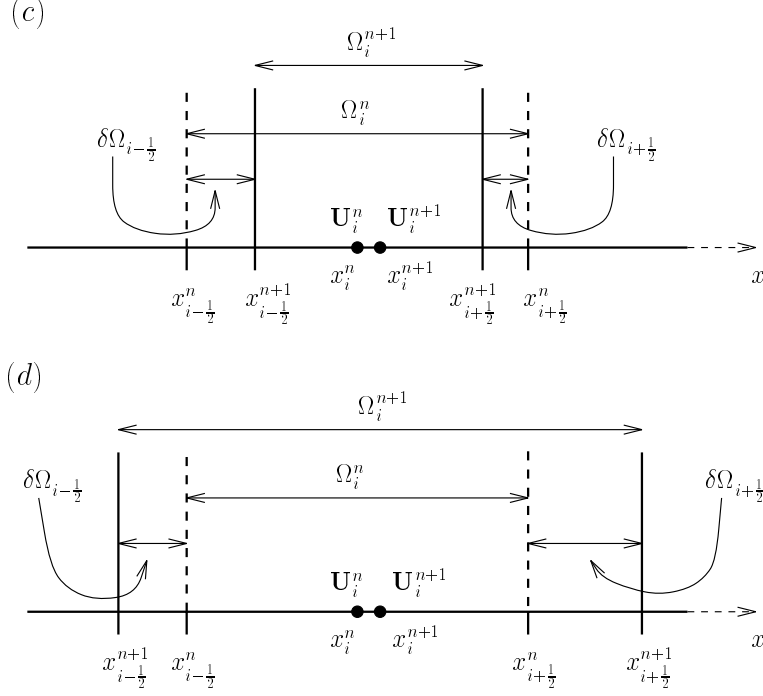


Figure 6: $x - U$ diagrams for cell I_i of cell contraction and expansion resulting from the Lagrangian phase.

$\dot{x}_{i-\frac{1}{2}}$ and are dependent on the type of data reconstruction applied in each cell.

As discussed earlier, the rezoning phase can be viewed as an advection process. Interpreting equation (81) in this way, the quantity $\delta\Omega_{i-\frac{1}{2}}$ can be seen as a volume flux, and the components of the vector $\hat{\mathbf{F}}_{i-\frac{1}{2}}$ can be viewed as advection fluxes divided by the velocity normal to the corresponding boundary. That is

$$\hat{\mathbf{F}}_{i-\frac{1}{2}} = \frac{\mathbf{F}_{i-\frac{1}{2}}}{\dot{x}_{i-\frac{1}{2}}}, \quad (83)$$

where $\mathbf{F}_{i-\frac{1}{2}}$ is a vector of numerical advection fluxes which are to be evaluated. $\hat{\mathbf{F}}_{i-\frac{1}{2}}$ is known as a vector of effective fluxes. Moreover, expression (78) can be substituted directly into equation (81) to produce the more familiar form of the non-linear advection equation

$$\bar{\mathbf{U}}_i = \frac{\Omega_i^{n+1}}{\Omega_i} \left(\mathbf{U}_i^{n+1} + \frac{\Delta t}{\Omega_i^{n+1}} \left[\dot{x}_{i-\frac{1}{2}} \hat{\mathbf{F}}_{i-\frac{1}{2}} - \dot{x}_{i+\frac{1}{2}} \hat{\mathbf{F}}_{i+\frac{1}{2}} \right] \right). \quad (84)$$

From a practical view point the vector equation (81) can be written in the component-wise form

$$\bar{\rho}_i = \frac{M_i^{n+1} + \delta\Omega_{i-\frac{1}{2}}\hat{F}_{i-\frac{1}{2}}^\rho - \delta\Omega_{i+\frac{1}{2}}\hat{F}_{i+\frac{1}{2}}^\rho}{\Delta x_i^n} \quad (85)$$

$$\bar{u}_i = \frac{u_i^{n+1}M_i^{n+1} + \delta M_{i-\frac{1}{2}}\hat{F}_{i-\frac{1}{2}}^u - \delta M_{i+\frac{1}{2}}\hat{F}_{i+\frac{1}{2}}^u}{\bar{M}_i} \quad (86)$$

$$\bar{e}_i = \frac{e_i^{n+1}M_i^{n+1} + \delta M_{i-\frac{1}{2}}\hat{F}_{i-\frac{1}{2}}^e - \delta M_{i+\frac{1}{2}}\hat{F}_{i+\frac{1}{2}}^e}{\bar{M}_i} \quad (87)$$

where $M_i = \rho_i\Delta x_i$ is the mass in cell I_i , $\delta M_{i-\frac{1}{2}} = \delta\Omega_{i-\frac{1}{2}}\hat{F}_{i-\frac{1}{2}}^\rho$, and \hat{F}^ρ , \hat{F}^u and \hat{F}^e are respectively the effective fluxes for density, velocity and internal energy.

Two methods for evaluating the required flux values are considered, namely the piecewise-constant, or Courant, Isaacson and Rees (CIR) scheme [2], and the piecewise-linear advection scheme of Van Leer [14]. The effective flux for these methods [8] are, respectively

$$\hat{F}_{i-\frac{1}{2}}^{pc}(a_{i-1}, a_i, \dot{x}_{i-\frac{1}{2}}) = \begin{cases} a_{i-1} & \text{if } \dot{x}_{i-\frac{1}{2}} \geq 0 \\ a_i & \text{if } \dot{x}_{i-\frac{1}{2}} \leq 0 \end{cases}, \quad (88)$$

and

$$\hat{F}_{i-\frac{1}{2}}^{pl}(a_{i-1}, a_i, \dot{x}_{i-\frac{1}{2}}) = \begin{cases} a_{i-1} + \frac{\Delta a_{i-1}}{2\Delta x_{i-1}} \left(\Delta x_{i-1} - \dot{x}_{i-\frac{1}{2}}\Delta t \right) & \text{if } \dot{x}_{i-\frac{1}{2}} \geq 0 \\ a_i - \frac{\Delta a_i}{2\Delta x_i} \left(\Delta x_i + \dot{x}_{i-\frac{1}{2}}\Delta t \right) & \text{if } \dot{x}_{i-\frac{1}{2}} \leq 0 \end{cases} \quad (89)$$

where

$$\Delta a_i = \begin{cases} \alpha \cdot \text{sign}(a_{i+1} - a_{i-1}) & \text{if } \beta \geq 0 \\ 0 & \text{otherwise} \end{cases}, \quad (90)$$

$$\alpha = \min\left(\frac{1}{2}|a_{i+1} - a_{i-1}|, 2|a_{i+1} - a_i|, 2|a_i - a_{i-1}|\right), \quad (91)$$

$$\beta = (a_{i+1} - a_i)(a_i - a_{i-1}). \quad (92)$$

For linear advection, equation (89) is monotonicity preserving.

The rezoning equations are derived by assuming a particle's location is at the center of a cell. However, the actual position of a particle is not required for any of the remap calculations. Therefore, since the particles are

being remapped back to their initial position, equation (12) is made redundant when rezoning is carried out at each time step. A similar observation concerning boundary positions can be made, leaving it unnecessary for the values $x_{i-\frac{1}{2}}^{n+1}$, $i = 0, 1, \dots, M$ to be calculated and stored.

6 Interface Tracking

The aim of this section is to present in detail a method for improving the resolution of the numerical solution profile at a material interface. The technique, developed by the author, is designed to be used in conjunction with the Lagrange-Remap (split) schemes discussed previously in this paper, where the rezoning is performed at each time step.

In the current setting of the one-dimensional compressible Euler equations, Lagrangian schemes are credited with the ability to accurately capture moving material interfaces because they do not excessively smear the density profile. (See for example the results of Section 7 which were generated using Lagrangian versions of the HLLC and Roe approximate Riemann solvers). Moreover, when using a Lagrangian scheme it is clear which equation of state is valid in each of the computational cells in the domain.

The premiss behind the solution method is to allow a Lagrangian-type scheme at the interface to coexist with a split scheme for regions away from the interface. The approach is to maintain the alignment of a cell boundary with the material interface throughout execution of the numerical scheme. The designated boundary then moves in a Lagrangian sense, i.e with the fluid, tracking the movement of the material interface. The alignment of the cell boundary with the interface is ensured by, firstly, permitting the existence of two non-uniform computational cells either side of the interface, and secondly, suppressing the remap procedure at the boundary coinciding with the interface. To prevent the creation of disproportionate non-uniform cell volumes and interaction between the interface and another boundary in the domain, the remap procedure of Section 5 is augmented with a reconstruction algorithm. The volume of ‘proportionate’ non-uniform cells are chosen by the author to be between one half and three halves of the volume of a uniform cell.

Tracking the interface in this way avoids the complications associated with multimaterial cells. Multimaterial cells do not exist at the initial time level, and they are not created during execution of the scheme.

The solution method is now described in detail.

The Initial Discretisation.

At an initial time $t = t^0$, a material interface is assumed to be located at position x_{ip} , and the computational domain is divided into M uniform computational cells of size Δx , as detailed in Section 2. If x_{ip} coincides with a cell boundary then cell averaged values of the conserved variables can be calculated for each cell and stored at their centre.

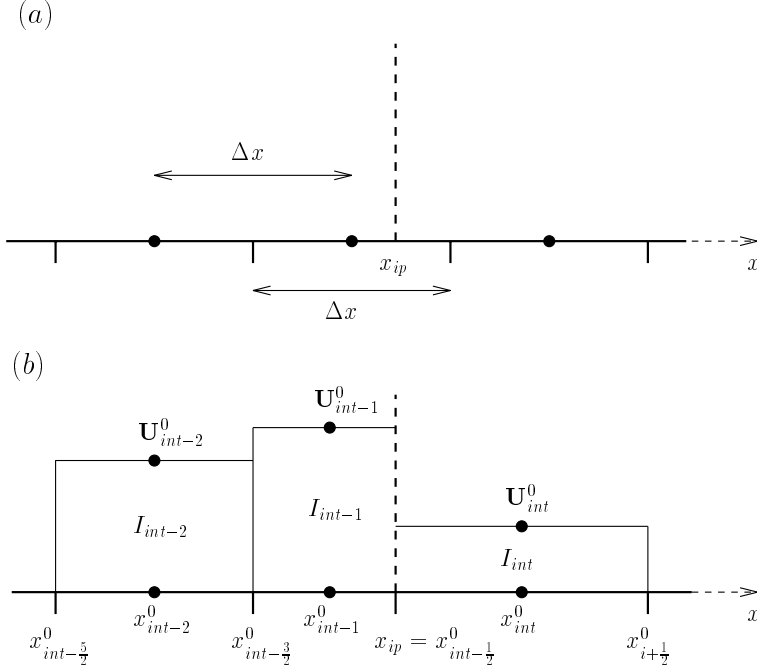


Figure 7: $x - U$ diagrams illustrating initial cell merging to the right of the material interface.

If x_{ip} does not initially coincide with a cell boundary, then the methodology is to form two non-uniform computational cells either side of the interface, forcing x_{ip} to be aligned with a boundary of the mesh. Then to ensure the newly created cells are proportionate the non-uniform cell with volume less than $\frac{1}{2}\Delta x$ ¹ is merged with its adjacent uniform cell. The boundary coinciding with x_{ip} is denoted $x_{int-\frac{1}{2}}$ and the cells to the left and right of $x_{int-\frac{1}{2}}$ are denoted I_{int-1} and I_{int} respectively. A schematic of this procedure is shown in Figures 7 and 8. Figure 7 shows the case where cell merging is required to the left of the interface. Figure 8 demonstrates cell merging on the right of

¹If x_{ip} is located in the exact centre of a cell, then one of the non-uniform cells is chosen arbitrarily.

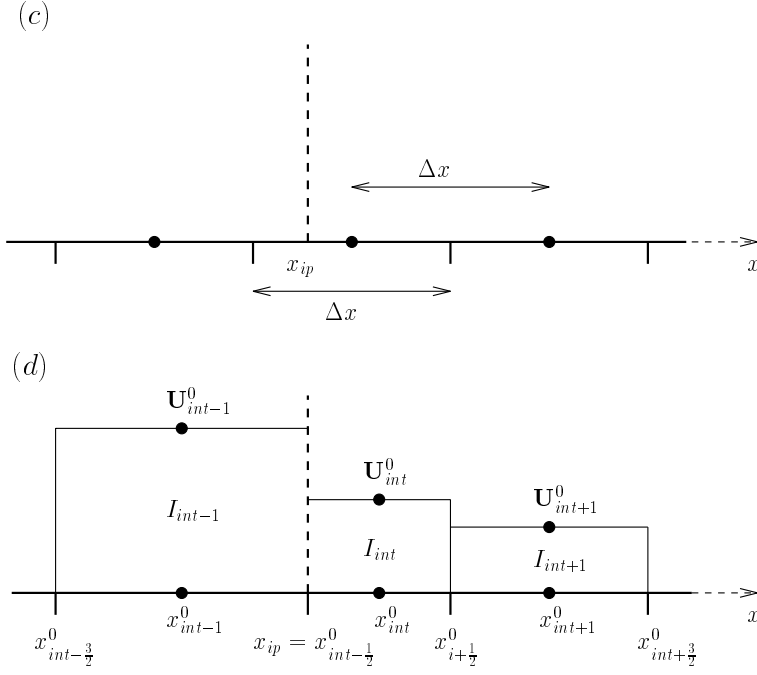


Figure 8: $x - U$ diagrams illustrating initial cell merging to the left of the material interface.

the interface. It should be noted that the number of cells in the computation domain has not been increased or decreased as a result of the reconstruction.

The Lagrangian and Remap Phases.

The Lagrangian phase of the split scheme is executed in exactly the same way as described in earlier sections, with a Riemann problem being solved approximately at the material interface. As with all cell boundaries, the position of $x_{int-\frac{1}{2}}$ (and hence the position of the interface) is updated via

$$x_{i-\frac{1}{2}}^{n+1} = x_{i-\frac{1}{2}}^n + \Delta t u_{i-\frac{1}{2}}, \quad (93)$$

where $u_{i-\frac{1}{2}}$ is an approximation of the fluid velocity normal to the boundary $x_{i-\frac{1}{2}}$ resulting from the Riemann solver. Thus, the interface boundary is explicitly updated by the equation

$$x_{ip}^{\text{new}} = x_{ip}^{\text{old}} + \Delta t u_{int-\frac{1}{2}}. \quad (94)$$

The mesh resulting from the Lagrangian phase is remapped following the approach described in Section 5. However, when rezoning, the the cell

boundary which is aligned with the material interface is not remapped. The boundary $x_{int-\frac{1}{2}}$ remains where it was positioned at the end of the Lagrangian phase. Therefore, at the end of the remap phase there continues to exist, embedded within an otherwise uniform grid, two non-uniform cells lying either side of the interface. Figure 9 contains $x - U$ diagrams illustrating the Lagrangian and amended remap phases at the interface for $u_{int-\frac{1}{2}} > 0$. The overbar is used to denote post-remap values.

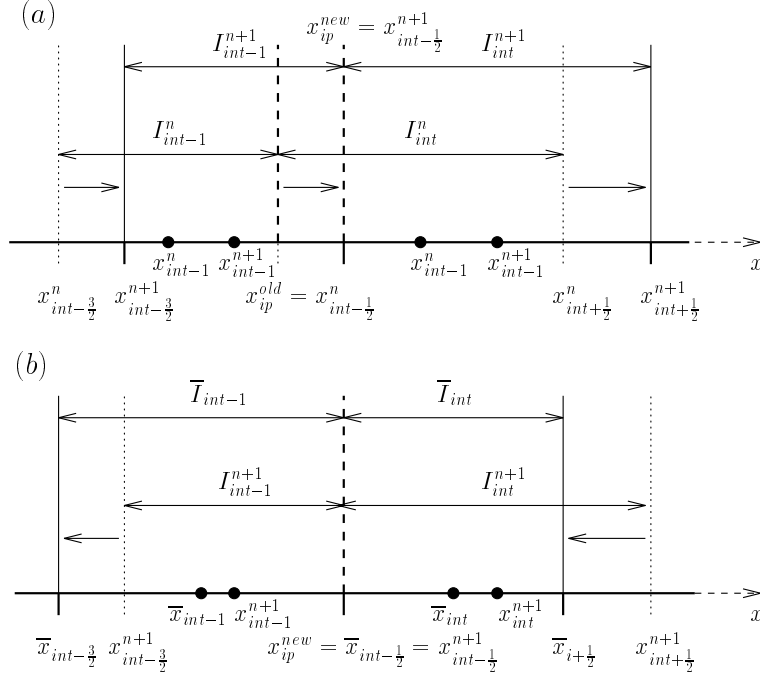


Figure 9: $x - U$ diagrams illustrating in (a) the Lagrangian phase and in (b) the amended remap procedure at the material interface when $u_{int-\frac{1}{2}} > 0$.

Reconstruction

To prevent the creation of disproportionate non-uniform cell volumes and interaction between the interface and another boundary of the computational domain, the remap procedure is augmented with a reconstruction algorithm.

The reconstruction need only be applied when the inequality

$$\frac{1}{2}\Delta x \leq \Delta \bar{x}_{int-1}^{n+1}, \Delta \bar{x}_{int}^{n+1} \leq \frac{3}{2}\Delta x, \quad (95)$$

is compromised.

The reconstruction process can be divide into two stages. The first stage is the merging of the non-uniform cell with volume less than $\frac{1}{2}\Delta x$ with its adjacent non-uniform cell. The second stage involves dividing the non-uniform cell with volume greater than $\frac{3}{2}\Delta x$ into a smaller non-uniform cell and a uniform mesh cell. By definition the smaller non-uniform cell will have volume $\Delta\bar{x}_i - \Delta x > \frac{1}{2}\Delta x$, satisfying inequality (95) ($i = int-1$ or int according to the value of $u_{int-\frac{1}{2}}$ (see below)). Intuitively, the direction in which the interface moves during the Lagrangian phase (indicated by the sign of $u_{int-\frac{1}{2}}$) will determine which cells are to be merged and which are to be divided. The result of the reconstruction will be two non-uniform cells \check{I}_{int-1} and \check{I}_{int} , satisfying (95), located either side of the interface and embedded within an uniform grid whose cells have volume Δx . The inverted hat symbol is used to indicate reconstructed quantities. The new discretization will have the same number of computational cells as the initial discretization. By definition,

$$x_{ip}^{new} = x_{int-\frac{1}{2}}^{n+1} = \bar{x}_{int-\frac{1}{2}} = \check{x}_{int-\frac{1}{2}}. \quad (96)$$

Cell Merging

If the material interface traverses the x -axis from left to right during the Lagrangian phase ($u_{int-\frac{1}{2}} > 0$) then it is necessary to merge cells I_{int}^{n+1} and I_{int+1}^{n+1} to form a new non-uniform cell \check{I}_{int} , see Figure 10. However, if in the Lagrangian phase the material interface progresses along the x -axis from right to left ($u_{int-\frac{1}{2}} < 0$) then it is necessary to merge cells I_{int-2}^{n+1} and I_{int-1}^{n+1} to create a new non-uniform cell \check{I}_{int-1} , see Figure 11. Cell volumes and node positions are updated via

$$\Delta\check{x}_{int+k} = \Delta\bar{x}_{int+k} + \Delta x, \quad (97)$$

$$\check{x}_{int+k} = \frac{x_{ip}^{new} + \bar{x}_{int+\frac{3}{2}+4k}}{2}, \quad (98)$$

where

$$k = \begin{cases} 0 & u_{int-\frac{1}{2}} > 0 \\ -1 & u_{int-\frac{1}{2}} < 0 \end{cases}. \quad (99)$$

The new conserved variable cell averages are evaluated using the formula

$$\check{\mathbf{U}}_{int+k} = \frac{\Delta\bar{x}_{int+k}\bar{\mathbf{U}}_{int+k} + \Delta x\bar{\mathbf{U}}_{int+1+3k}}{\Delta\check{x}_{int+k}}, \quad (100)$$

where k is given by equation (99).

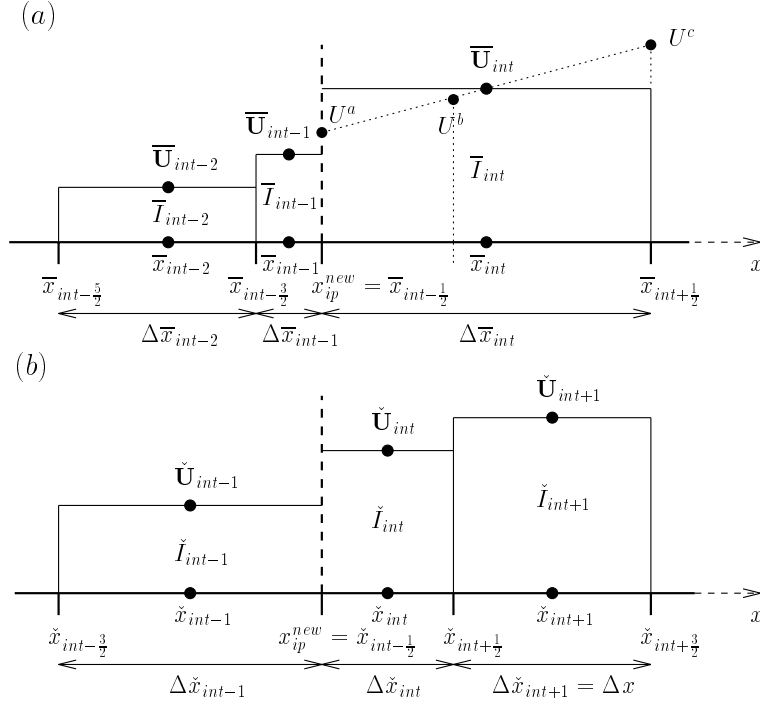


Figure 11: $x - U$ diagram illustrating cell reconstruction for $u_{int-\frac{1}{2}} < 0$.

cell boundaries and node positions are updated via

$$\Delta \check{x}_{int-1-k} = \Delta \bar{x}_{int-1-k} - \Delta x, \quad (101)$$

$$\Delta \check{x}_{int-2-3k} = \Delta x, \quad (102)$$

$$\check{x}_{int-\frac{3}{2}-2k} = \begin{cases} x_{ip}^{new} - \Delta \check{x}_{int-1} & k = 0 \\ x_{ip}^{new} + \Delta \check{x}_{int} & k = -1 \end{cases}, \quad (103)$$

$$\check{x}_{int-1-k} = \frac{\check{x}_{int-\frac{3}{2}-2k} + x_{ip}^{new}}{2}, \quad (104)$$

$$\check{x}_{int-2-3k} = \check{x}_{int-\frac{5}{2}-3k} + \frac{\Delta x}{2}, \quad (105)$$

where k is given by equation (99).

Within the non-uniform cell to be divided, the piecewise constant data cell average values $\bar{U}_{int-1-k}$ are locally replaced by piecewise linear functions according to

$$\bar{U}_{int-1-k}(x) = \bar{U}_{int-1-k} + (x - \bar{x}_{int-1-k}) \sigma_{int-1-k}, \quad x \in [\bar{x}_{int-\frac{3}{2}-k}, \bar{x}_{int-\frac{1}{2}-k}], \quad (106)$$

where $\sigma_{int-1-k}$ is a vector of limited first derivative approximations, and k is given by equation (99). The vector $\sigma_{int-1-k}$ is taken to be a function of the vectors $\left(\frac{\overline{\Delta}_{int-\frac{3}{2}-2k}}{\Delta\overline{x}_{int-\frac{3}{2}-2k}}\right)$ and $\left(\frac{\overline{\Delta}_{int-\frac{5}{2}-4k}}{\Delta\overline{x}_{int-\frac{5}{2}-4k}}\right)$, namely

$$\sigma_{int-1-k} = \sigma_{int-1-k} \left(\frac{\overline{\Delta}_{int-\frac{3}{2}-2k}}{\Delta\overline{x}_{int-\frac{3}{2}-2k}}, \frac{\overline{\Delta}_{int+\frac{5}{2}-4k}}{\Delta\overline{x}_{int+\frac{5}{2}-4k}} \right), \quad (107)$$

where

$$\overline{\Delta}_{int-\frac{3}{2}-2k} = \overline{\mathbf{U}}_{int-1-2k} - \overline{\mathbf{U}}_{int-2-2k} \text{ and} \quad (108)$$

$$\overline{\Delta}_{int-\frac{5}{2}-4k} = \overline{\mathbf{U}}_{int-2-4k} - \overline{\mathbf{U}}_{int-3-4k}. \quad (109)$$

The components of $\sigma_{int-1-k}$ are evaluated using the formula

$$\min \text{ mod} \left(\frac{\overline{\Delta}_{i-\frac{3}{2}-2k}^{(j)}}{\Delta\overline{x}_{i-\frac{3}{2}-2k}}, \frac{\overline{\Delta}_{i-\frac{5}{2}-4k}^{(j)}}{\Delta\overline{x}_{i-\frac{5}{2}-4k}} \right), \quad (110)$$

where $\overline{\Delta}_{i-\frac{3}{2}-2k}^{(j)}$ is the j^{th} ($j = 1, 2, 3$) component of $\overline{\Delta}_{i-\frac{3}{2}-2k}$, and

$$\min \text{ mod} (x, y) = \frac{1}{2} (\text{sign}(x) + \text{sign}(y)) \min (|x|, |y|), \quad (111)$$

$$\text{sign} = \frac{x}{|x|}. \quad (112)$$

The values of $\overline{\mathbf{U}}_{int-1-k}(x)$ at the boundaries $\check{x}_{int-\frac{5}{2}-2k}$, $\check{x}_{int-\frac{3}{2}-2k}$ and $\check{x}_{int-\frac{1}{2}-2k}$ are, respectively

$$\mathbf{U}^a = \overline{\mathbf{U}}_{int-1-k} - \frac{\Delta\overline{x}_{int-1-k}}{2} \sigma_{int-1-k}, \quad (113)$$

$$\mathbf{U}^b = \overline{\mathbf{U}}_{int-1-k} + \left(\check{x}_{int-\frac{3}{2}-2k} - \overline{x}_{int-1-k} \right) \sigma_{int-1-k} \quad \text{and} \quad (114)$$

$$\mathbf{U}^c = \overline{\mathbf{U}}_{int-1-k} + \frac{\Delta\overline{x}_{int-1-k}}{2} \sigma_{int-1-k}. \quad (115)$$

Redistribution of the conserved variables is then equivalent to evaluating the area of the trapezoids which lie above the respective cells and below the piecewise linear function, see Figures 10 and 11. Cell averages values, which are to be stored at the cell centre, are obtained upon division by the corresponding volume. Therefore

$$\check{\mathbf{U}}_{int-1-2k} = \frac{1}{\Delta\check{x}_{int-1-2k}} \cdot \frac{\Delta\check{x}_{int-1-2k}}{2} (\mathbf{U}^b + \mathbf{U}^c), \quad (116)$$

$$\check{\mathbf{U}}_{int-2-2k} = \frac{1}{\Delta\check{x}_{int-2-2k}} \cdot \frac{\Delta\check{x}_{int-2-2k}}{2} (\mathbf{U}^a + \mathbf{U}^b), \quad (117)$$

where k is given by equation (99).

7 Numerical Results

The selected test problems are shock tube problems [9], [8]. The premiss of the problem is a long cylindrical tube containing two mediums separated initially by a thin membrane. The materials are assumed to be at rest, but are held at different constant pressures and densities. At time t^0 the membrane is ruptured and the problem is to determine the ensuing motion of the two materials.

In this work, the materials either side of the membrane (and the ensuing material interface) are ideal gases, and the ideal gas equation of state is employed as the closure condition for the governing equations (see section 1). An ideal gas is uniquely determined by the value of γ , the ratio of specific heat capacities of the fluid, in the equation of state.

Numerically, the initial conditions of the test consist of two constant states separated by a discontinuity. The two states are given by

$$\begin{pmatrix} \rho_L \\ u_L \\ p_L \end{pmatrix} \quad \text{and} \quad \begin{pmatrix} \rho_R \\ u_R \\ p_R \end{pmatrix} \quad (118)$$

The discontinuity is initially situated at $x = 0.5$. The values of γ to the left and to the right of the material interface is denoted by γ_L and γ_R respectively. Three test problems are considered, each with an exact solution for the one dimension time dependent Euler equations. The initial data for the tests is given in table 1. The exact solution for each of the tests consists of a left travelling rarefaction wave, and right travelling contact and shock waves. The exact and numerical solutions are computed in the spatial domain $0 \leq x \leq 1$. The numerical solution is computed with $M = 100$ cells, and boundary conditions are transmissive. In the figures displaying results, the exact solution is represented by a full line and the numerical solution is denoted by a dotted line.

	ρ_L	u_L	p_L	γ_L	ρ_R	u_R	p_R	γ_R
test 1	1.0	0.0	1.0	1.4	0.125	0.0	0.1	1.4
test 2	1.0	0.0	1.0	1.4	0.125	0.0	0.1	1.2
test 3	1.0	0.0	1.0	1.6	0.125	0.0	0.1	1.2

Table 1: Initial data for the tests 1 to 3

Four sets of results are presented. Figures 12 to 20 display the results produced using the Eulerian, or unsplit fixed grid, versions of the HLLC and Roe schemes studied in this paper, as applied to test 1. They are included for

comparative reasons and full details of their implementation can be found in the book by E. F. Toro [12]. Figures 21 to 29 show the results generated by the Lagrangian HLLC and Roe schemes, as applied to test 1. As a consequence of the simplicity of the test problem, (i.e one-dimension, no wave interactions and small temporal domain), there is no mesh tangling (node over taking in one-dimension). Hence the Lagrangian results presented suffer from none of the inaccuracies caused by grid distortion, and serve as a valuable comparison to the Lagrange-Remap data. Figures 30 to 47 contain the results created using the Lagrange-Remap, or split fixed grid, HLLC and Roe methods, as applied to test 1. Figures 48 to 53 show the results from the second order HLLC scheme with a piecewise linear remap procedure, as applied to tests 1 to 3.

Eulerian Methods.

The results from the first-order HLLC and Roe schemes are displayed in Figures 12 and 13 respectively. Both figures show poor resolution of the nonlinear waves and the discontinuous character of the linear wave is unrecognizable. There are no signs of spurious oscillations in either of the results.

The results from the second-order HLLC and the Roe schemes are presented in Figures 14 to 20. Figures 14 to 17 show results for the HLLC method using slope limiters which are ‘equivalent’ to the flux limiters minbee and superbee. Figures 18 to 20 display the results obtained using the flux limited version of Roe’s scheme with the minbee, Van Leer and superbee flux limiters. All the plots disclose an anticipated improvement in accuracy upon the corresponding first-order results.

The HLLC results generated using conserved variable slope limiting (Figures 14 and 15) contain spurious oscillations between the right travelling contact and shock waves. Particularly visible is the erroneous fluctuation in the results corresponding to the superbee slope limiter. In comparison, the HLLC results produced using wave-by-wave slope limiting (Figures 16 and 17) are void of spurious oscillations. Apart from this discrepancy, the two approaches produce solution profiles of equal accuracy. Hence, the data appears to suggest that it is advantageous to apply wave-by-wave limiting, rather than to employ conserved variable limiting in an Eulerian reference frame.

Regardless of the type of slope limiting, the superbee limiter gives rise to sharper resolution of the shock and rarefaction discontinuities than the minbee limiter.

The second order Roe results are bereft of fluctuations and the shock discontinuity is sharply resolved. The results from the superbee limiter are

the most promising, producing the most accurate solution profile of the three limiters studied. The superiority of the van Leer limiter over the minbee limiter, is also demonstrated.

Lagrangian Methods.

The results from the first-order HLLC and Roe schemes are presented in Figures 21 and 22 respectively. Both figures show equally poor shock resolution, smearing the profile across six cells. The contact discontinuity is captured well by both of the schemes, with the HLLC method exhibiting a slightly sharper resolution. The HLLC results contain an overshoot immediately ahead of the contact discontinuity, whilst in the Roe results an oscillation is visible directly behind the contact wave. Diffusion of the rarefaction wave, typical of that expected by first-order schemes, is visible in both figures. The Roe scheme achieves greater accuracy at the shock wave than the HLLC scheme.

The results from the second-order HLLC and the Roe schemes are displayed in Figures 23 to 29. Figures 23 to 26 show results for the HLLC method using slope limiters which are ‘equivalent’ to the flux limiters minbee and superbee. Figures 27 to 29 present the results obtained using the flux limited version of Roe’s scheme with the minbee, Van Leer and superbee flux limiters. All the plots show an anticipated improvement in accuracy upon the corresponding first-order results.

The HLLC results generated using conserved variable slope limiting (Figures 23 and 24) display spurious oscillation between the contact and shock discontinuities. On the other hand the HLLC results produced using wave-by-wave slope limiting (Figures 25 and 26) show only a single overshoot ahead of the contact wave. Hence, the data appears to indicate an advantage in using wave-by-wave slope limiting oppose to conserved variable limiting in a Lagrangian reference frame.

Regardless of which slope limiting process is applied, the superbee limiter induces greater accuracy across the shock and rarefaction waves than the minbee limiter.

Each of the second-order Roe results contain an oscillation preceding the contact discontinuity. The results from the superbee flux limiter show an accurate capturing of discontinuities, however oscillations are visible behind the shock wave, see Figure 29. In comparison, the results from the minbee flux limiter do not contain spurious oscillations behind the shock wave, however the solution profile suffers greater smearing, see Figure 27. The van Leer flux limiter produces results which lie between these two extremes, see Figure 28.

Lagrange-Remap Methods.

The results from the first-order HLLC and Roe schemes are given in Figures 30 to 33. Figures 30 and 31 are a consequence of applying a piecewise constant remap, whilst Figures 32 and 33 result from using a piecewise linear remap.

The piecewise constant results show no signs of spurious oscillations. There is considerable smearing of discontinuities, most noticeable across the contact wave, as highlighted on the density and energy plots. The Roe scheme achieves greater accuracy at the shock wave than the HLLC scheme.

The piecewise linear results demonstrate an expected increase in accuracy over the piecewise constant results. However, spurious oscillations are visible in the figures between the contact and shock waves. These fluctuations are certainly more profound within the Roe results, where there exists a substantial oscillation behind the shock discontinuity.

The results from the second-order HLLC and Roe schemes are displayed in Figures 34 to 47. Figures 34 to 40 present results with a piecewise constant remap, whilst Figures 41 to 47 show results created by applying a piecewise linear remap. All the results indicate an anticipated advance in accuracy across discontinuities caused by increasing the order accuracy of the Lagrangian phase.

For the HLLC scheme with a piecewise constant remap, the second-order results are void of oscillations. The contact discontinuity is poorly resolved in each of the figures. The results again reveal the advantage of using a superbee limiter instead of a minbee limiter. i.e. sharper resolution of the nonlinear waves. However, these results also show a visible drop in the height of the solution profile, between the contact and shock discontinuities, when replacing the minbee limiter with the superbee limiter.

The results for the Roe scheme with a piecewise constant remap exhibit erroneous oscillations behind the shock wave. Unsatisfactory contact resolution is also evident. From looking at the results, it is obvious that the superbee flux limiter generates the sharpest discontinuities, but contain the most violent oscillations. The minbee flux limiter creates the most smeared solution profile, but produces the smallest oscillations. The van Leer limiter results again fall between these two extremes. The drop in profile height, between the contact and shock waves, is also apparent in the Roe results when using the superbee limiter as opposed to the minbee limiter.

As with the first-order schemes, the results show an expected improvement in accuracy when the constant remap is replaced by a piecewise linear remap. However, spurious oscillations are introduced into the HLLC results and the fluctuations in the Roe data are amplified. The Figures 41 to 47 con-

firm that there is a reduction in the height of the solution profile, between the contact and shock discontinuities, when minbee (slope or flux) limiter is replaced by a superbee limiter.

The benefits of using wave-by-wave slope limiting instead of conserved slope limiting are less obvious when either of the remapping methods is employed.

Eulerian Method Vs Lagrange-Remap Method

The results from the first-order HLLC and Roe Eulerian schemes are displayed in Figures 12 and 13 respectively. These are comparable to the results produced by first-order HLLC and Roe Lagrangian methods with a piecewise constant remap, which are located in Figures 30 and 31 respectively.

As visible, both the HLLC and the Roe unsplit (Eulerian) results demonstrate greater accuracy across the non-linear discontinuities, than the corresponding split (Lagrange-Remap) results. Particularly apparent is the difference in the resolution profiles at the rarefaction wave. The discontinuous character of the linear wave is unrecognisable with both the unsplit and split results.

The results from the second-order Eulerian HLLC and Roe schemes are presented in Figures 14 to 20. Figures 14 to 17 show results for the HLLC method using slope limiters. While Figures 18 to 20 present the results obtained using the flux limited version of Roe's scheme. These plots are comparable to the results generated using the second-order HLLC and Roe Lagrangian methods with a piecewise linear remap, which can be found in Figures 41 to 47.

For the HLLC scheme the superiority, in this test problem, of the wave-by-wave slope limiting over the conserved variable limiting has been established in the previous discussions. Therefore, the following observations are related to those results created using wave-by-wave slope limiting only (see Figures 16 and 17 for the unsplit results, and Figures 43 and 44 for the split results).

Limiter-wise the HLLC method achieves the same level of accuracy across the non-linear waves for the split and unsplit approaches. However, Figures 16 and 43 indicate that the minbee limiter produces a sharper contact discontinuity when it is applied with a Lagrangian-Remap scheme as opposed to an Eulerian scheme. In contrast, the super limiter favours the unsplit setting over the split, producing a contact wave spread across 4 cells compared to 5 cells respectively (see Figures 17 and 44).

Regardless of which limiter is used, the results produced using the unsplit HLLC schemes are void of oscillations. However, the data corresponding to

the split HLLC methods show erroneous fluctuations between the shock and contact waves.

For the Roe scheme, limiter-wise it is visible that there is no obvious advantage in adopting either the unsplit or the split approaches when considering accuracy across the shock and rarefaction waves. However, the Lagrange-Remap results are polluted with large spurious oscillations which are not visible in the Eulerian data. Moreover, when considering the results from the Van Leer and superbee limiter, the contact resolution from the split scheme can be viewed as poor when compared to that of the unsplit scheme.

Interface Tracking Method

The results to tests 1 to 3, generated using the second-order HLLC scheme with a piecewise linear interface tracking remap procedure, are displayed in Figures 48 to 53. Figures 48, 50 and 52 show results created using a minbee slope limiter, while Figures 49, 51 and 53 contain those results produced using a superbee slope limiter.

The results from test 1, Figure 48 and 49, are directly comparable to the results in Figures 43 and 44, which were created using the second-order HLLC Lagrange scheme with a standard piecewise linear remap. As visible the interface tracking procedure has made a significant improvement to the solution profile at the interface. In Figures 48 and 49, there is no smearing of the contact discontinuity. However, in regions away from the interface there appears to be no difference between the two sets of data. In particular, there still exists in the density plots, diffusion to left of the contact and a slight undershoot to the right.

The characteristics of the interface tracking technique are echoed in the results from tests 2 and 3, see Figures 50 to 53.

8 Conclusions

The main focus of this work has been to numerically solve the Euler equations for one-dimensional unsteady compressible flow, by employing a finite volume Lagrange-Remap scheme. The rezoning is carried out at each time step and the mesh is remapped back to the grid which was used at the initial time level. The aim was to acquire an insight into whether or not there is any benefit to employing a split fixed grid scheme (Lagrange-Remap), rather than an unsplit fixed grid scheme (Eulerian), to solve the governing system of equations.

The results from the shock tube problem would seem to suggest that there is no obvious advantage in adopting a Lagrange-Remap approach over an Eulerian method. In fact the data would perhaps prompt the reader to disregard the option of using an split scheme altogether. However, to base a judgement on the results from one test problem alone would be, at best, naive. To make a more informed decision, it would be wise to consider a greater range of test problems in which there were wave interactions and dimensions greater than one.

The split scheme presents the opportunity to consider the solution for the sound wave related transport and the advection related transport separately. It is this authors opinion, that this decomposition offers greater potential for developing an accurate ‘fixed grid’ solution method, than when faced with the unsplit scenario. Moreover, in this work the results generated using the Lagrangian schemes were extremely promising, and in general achieved greater accuracy than the Eulerian results. It was only when the Lagrangian schemes were combined with a remap phase, that the results became less impressive than those from the Eulerian methods. Hence, the remap phase in this work could be viewed as over diffusive, and this author believes that an improvement in the rezoning algorithm would lead to the split scheme results surpassing the unsplit results in terms of accuracy.

For the Eulerian approach the most accurate solution profile was created by the flux-limited Roe scheme using the superbee limiter (see Figure 20). The most precise results generated by a Lagrangian scheme were those produced by the HLLC method with wave-by-wave slope limiting using the superbee limiter (see Figure 26). In terms of the Lagrange-Remap methods, the most accurate solution profile was created by the HLLC scheme using wave-by-wave slope limiting with superbee limiter and a piecewise linear remap (see Figure 44).

The interface tracking procedure of Section 6 has shown to greatly improve the resolution of the solution profile at the material interface. There is no smearing of the contact discontinuity. However, the method has not alleviated, from the density profile, the diffusion to the left of the contact and the undershoot to the right. Furthermore, extension to higher dimensions is not obvious.

9 Extensions

Areas of future work include a more rigorous testing of the proposed Lagrange-Remap solution method. This should involve investigating how the schemes cope with wave interactions, and how the methods can be implemented in

higher dimensions. In addition, there is scope for improving or even raising the order of accuracy of the existing Lagrange and Remap phases of the split scheme. For example, Sims [8] explored a piecewise parabolic (third order accurate) remap algorithm.

Alternative methods for accurately resolving a material interface in one and higher dimensions need to be investigated further.

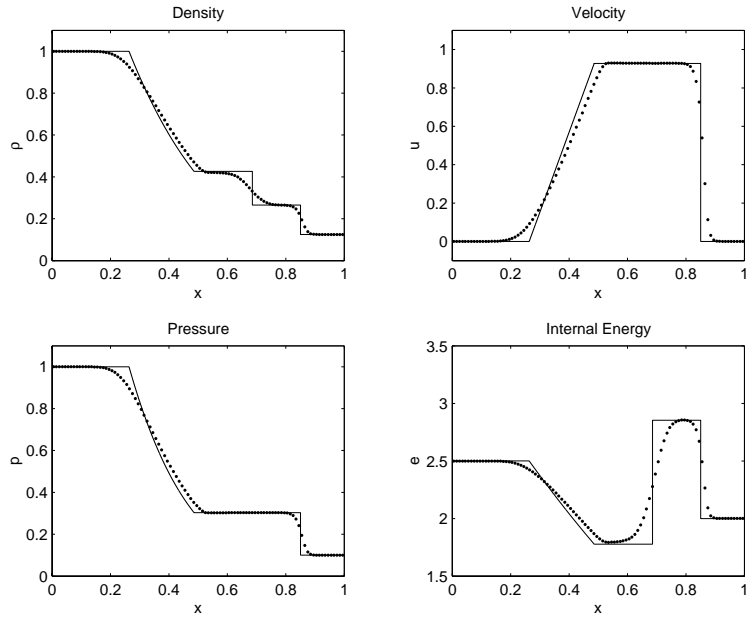


Figure 12: HLLC Eulerian method applied to test 1. Numerical (dotted line) and exact (solid line) solutions are evaluated at time 0.2 units.

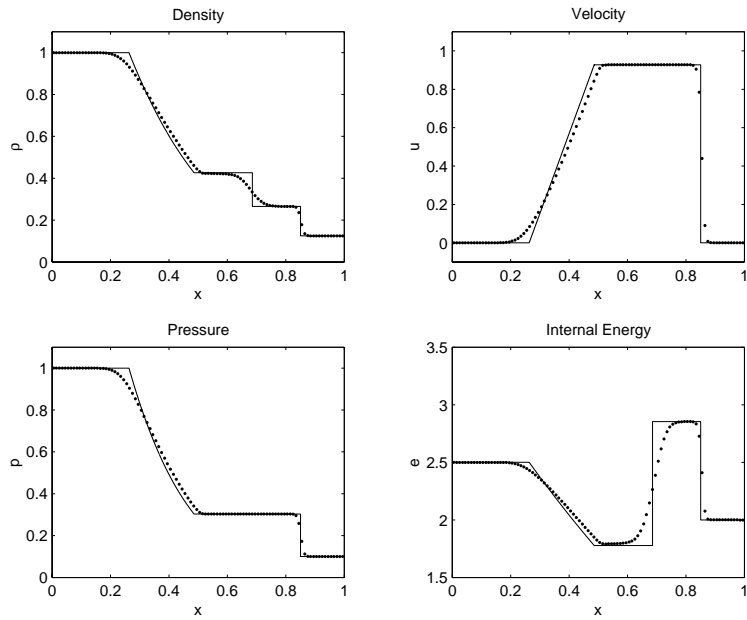


Figure 13: Roe Eulerian method applied to test 1. Numerical (dotted line) and exact (solid line) solutions are evaluated at time 0.2 units.

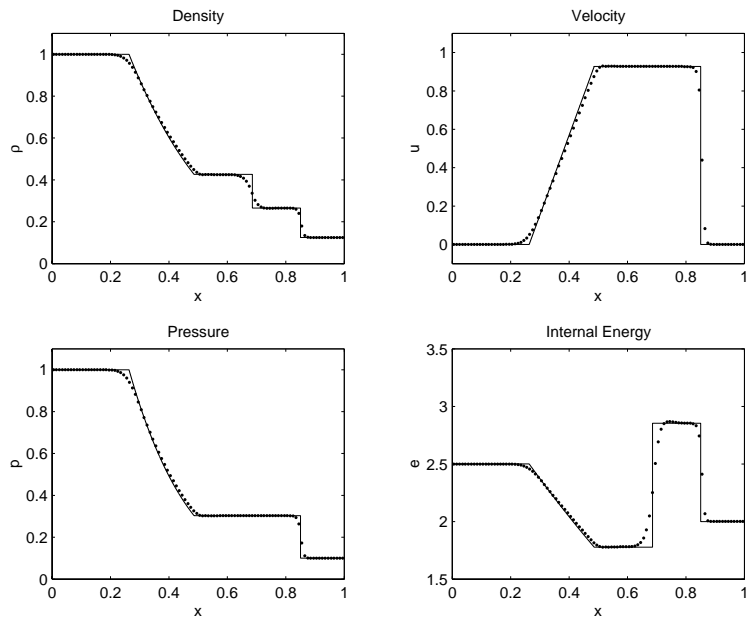


Figure 14: MUSCL-Hancock HLLC Eulerian method applied to test 1, with conserved variable slope limiting using the minbee limiter. Numerical (dotted line) and exact (solid line) solutions are evaluated at time 0.2 units.

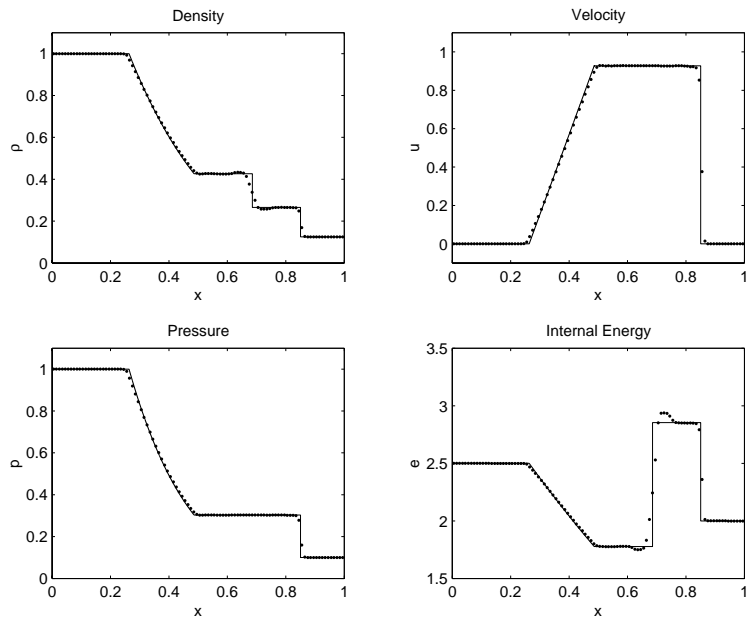


Figure 15: MUSCL-Hancock HLLC Eulerian method applied to test 1, with conserved variable slope limiting using the superbee limiter. Numerical (dotted line) and exact (solid line) solutions are evaluated at time 0.2 units.

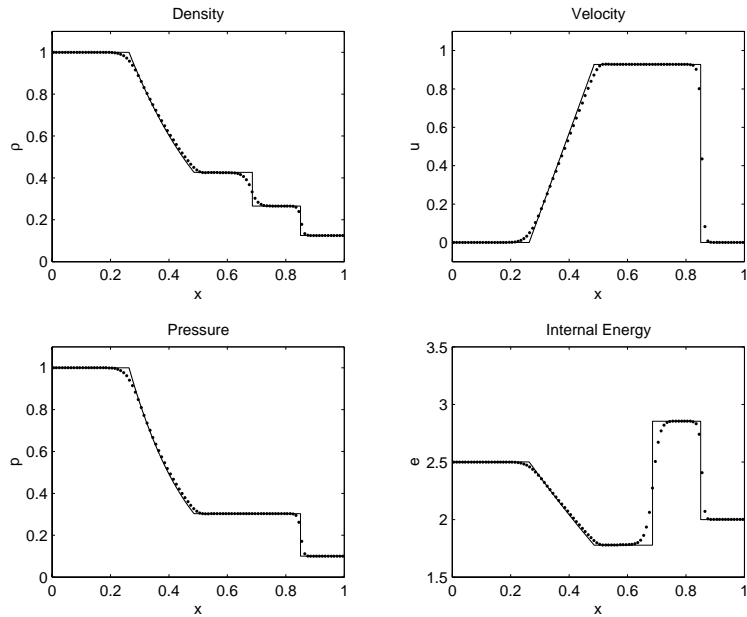


Figure 16: MUSCL-Hancock HLLC Eulerian method applied to test 1, with wave-by-wave slope limiting using the minbee limiter. Numerical (dotted line) and exact (solid line) solutions are evaluated at time 0.2 units.

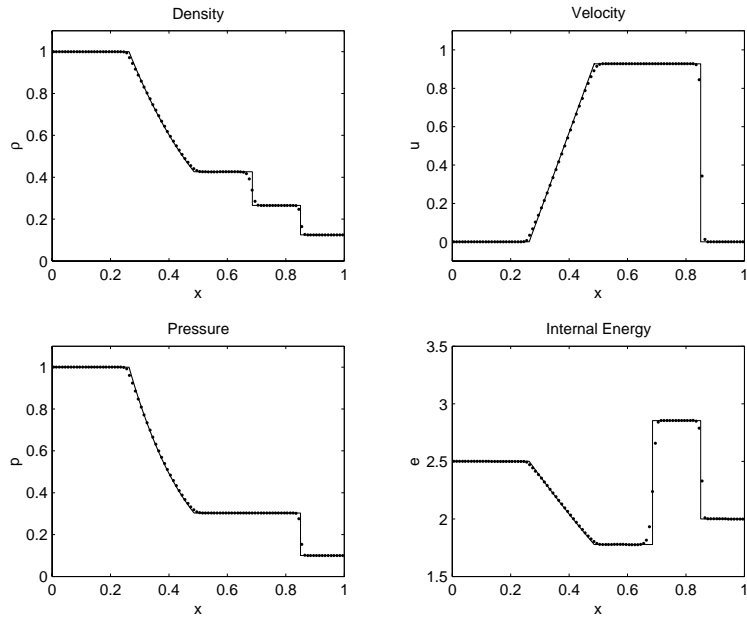


Figure 17: MUSCL-Hancock HLLC Eulerian method applied to test 1, with wave-by-wave slope limiting using the superbee limiter. Numerical (dotted line) and exact (solid line) solutions are evaluated at time 0.2 units.

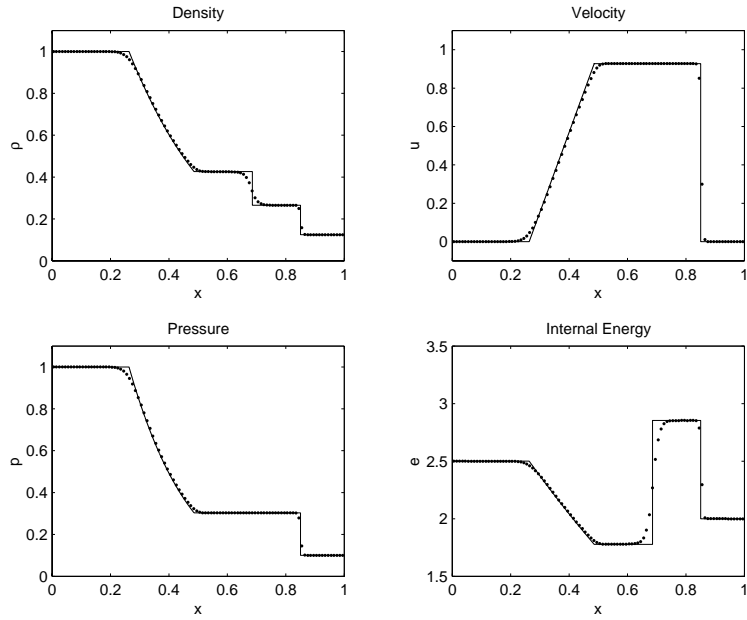


Figure 18: Flux limited version of Roe Eulerian method applied to test 1, using the minbee limiter. Numerical (dotted line) and exact (solid line) solutions are evaluated at time 0.2 units.

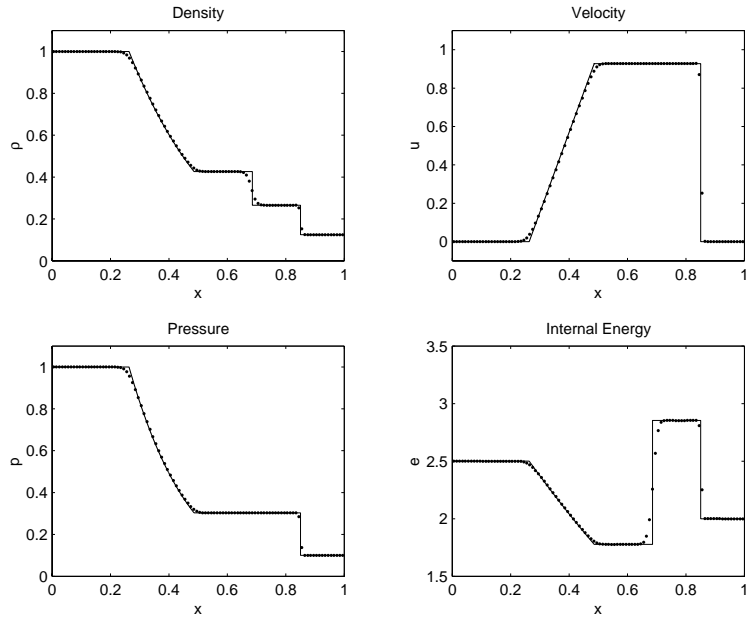


Figure 19: Flux limited version of Roe Eulerian method applied to test 1, using the Van Leer limiter. Numerical (dotted line) and exact (solid line) solutions are evaluated at time 0.2 units.

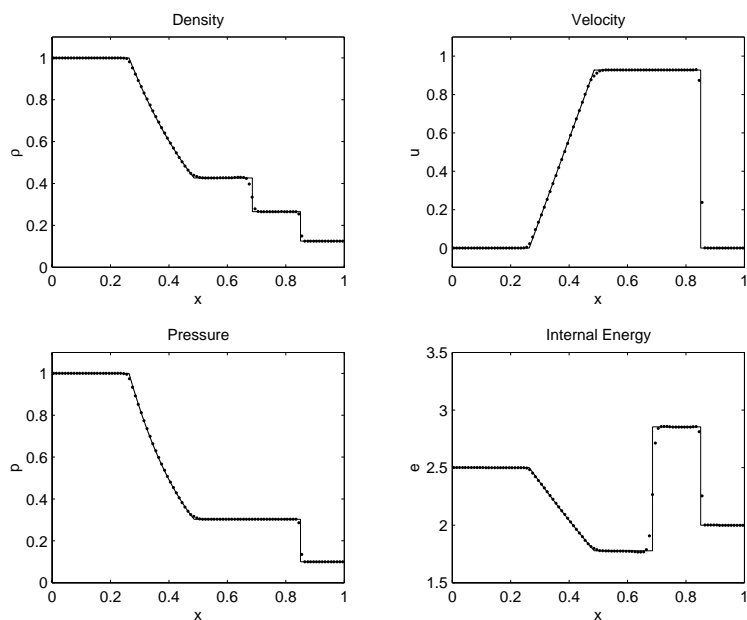


Figure 20: Flux limited version of Roe Eulerian method applied to test 1, using the superbee limiter. Numerical (dotted line) and exact (solid line) solutions are evaluated at time 0.2 units.

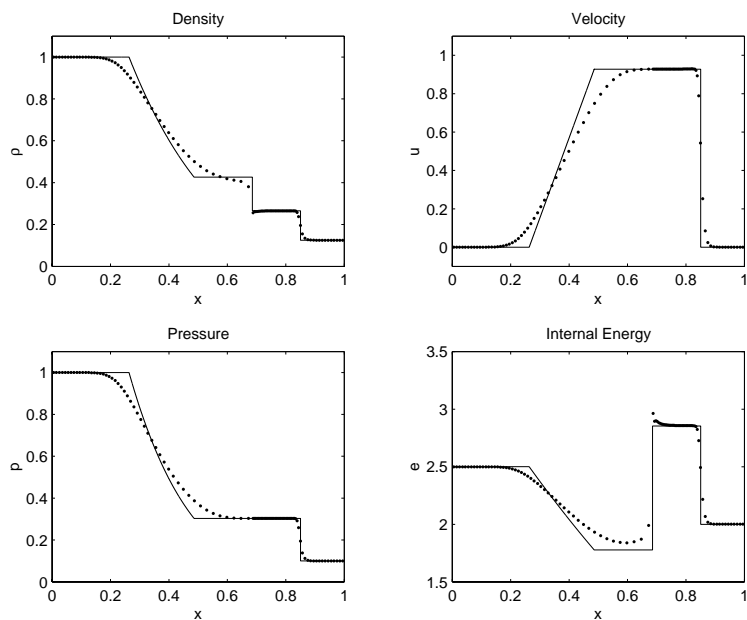


Figure 21: HLLC Lagrangian method applied to test 1. Numerical (dotted line) and exact (solid line) solutions are evaluated at time 0.2 units.

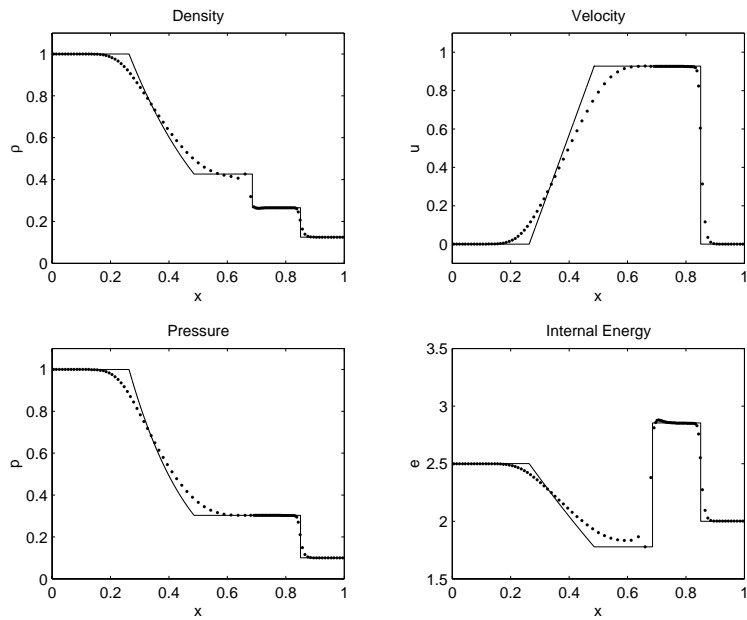


Figure 22: Roe Lagrange method applied to test 1. Numerical (dotted line) and exact (solid line) solutions are evaluated at time 0.2 units.

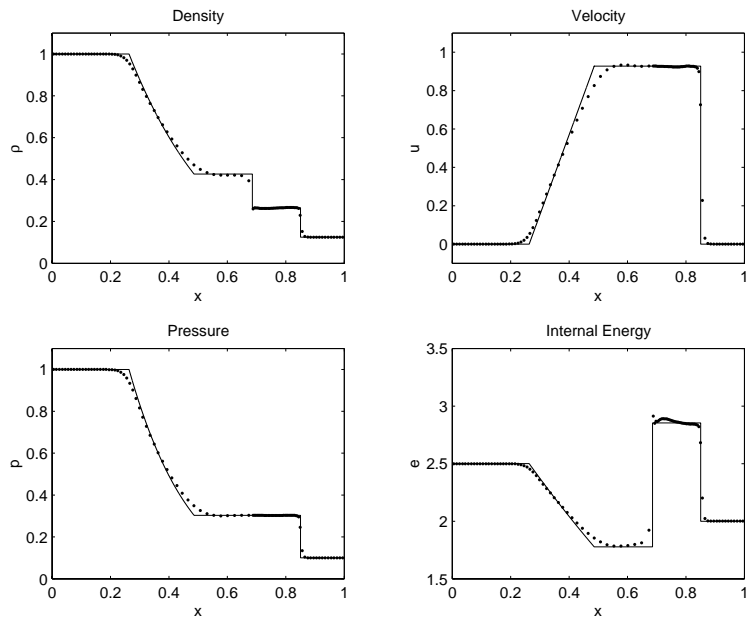


Figure 23: MUSCL-Hancock HLLC Lagrangian method applied to test 1, with conserved variable slope limiting using the minbee limiter. Numerical (dotted line) and exact (solid line) solutions are evaluated at time 0.2 units.

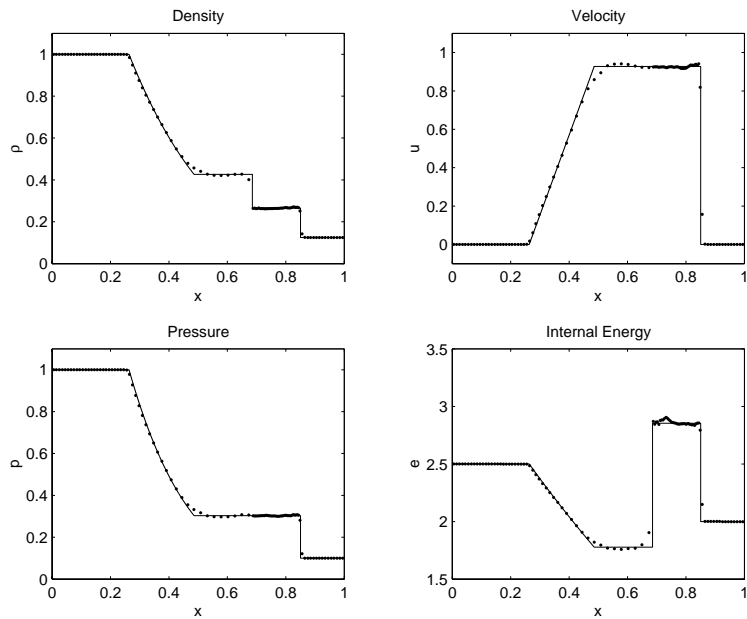


Figure 24: MUSCL-Hancock HLLC Lagrangian method applied to test 1, with conserved variable slope limiting using the superbee limiter. Numerical (dotted line) and exact (solid line) solutions are evaluated at time 0.2 units.

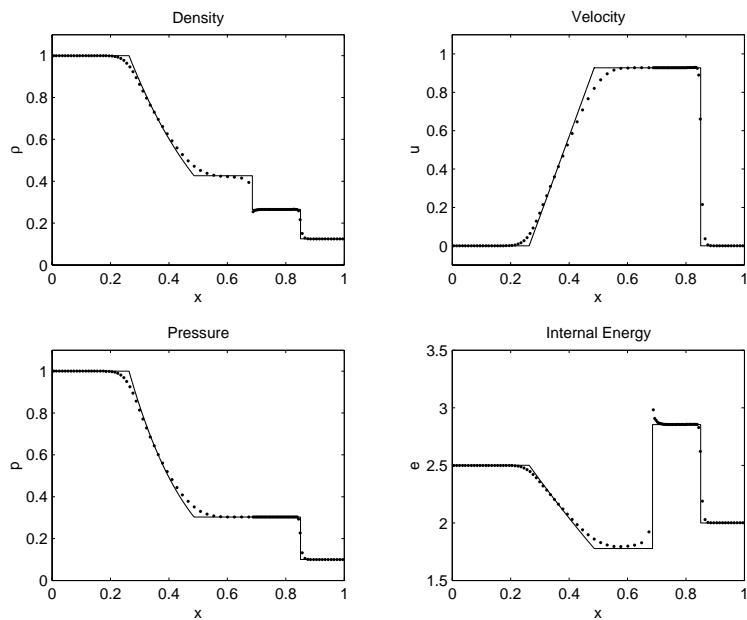


Figure 25: MUSCL-Hancock HLLC Lagrangian method applied to test 1, with wave-by-wave slope limiting using the minbee limiter. Numerical (dotted line) and exact (solid line) solutions are evaluated at time 0.2 units.

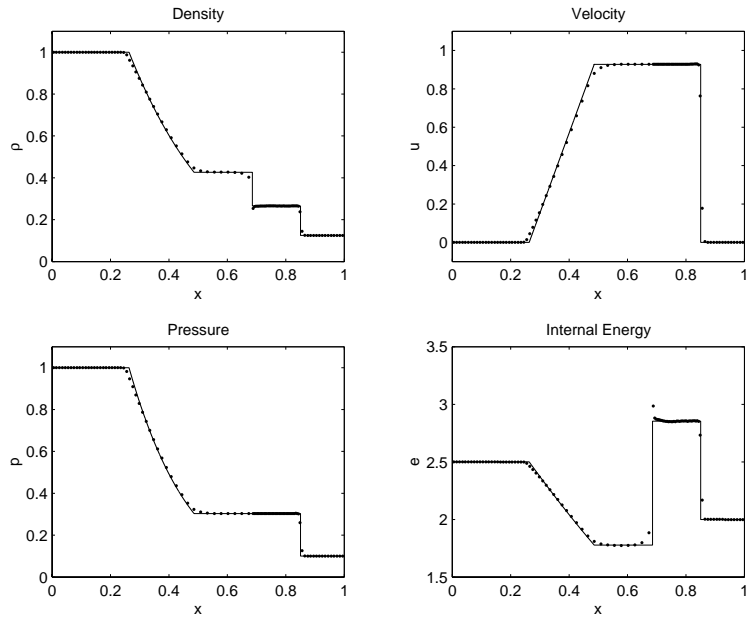


Figure 26: MUSCL-Hancock HLLC Lagrangian method applied to test 1, with wave-by-wave slope limiting using the superbee limiter. Numerical (dotted line) and exact (solid line) solutions are evaluated at time 0.2 units.

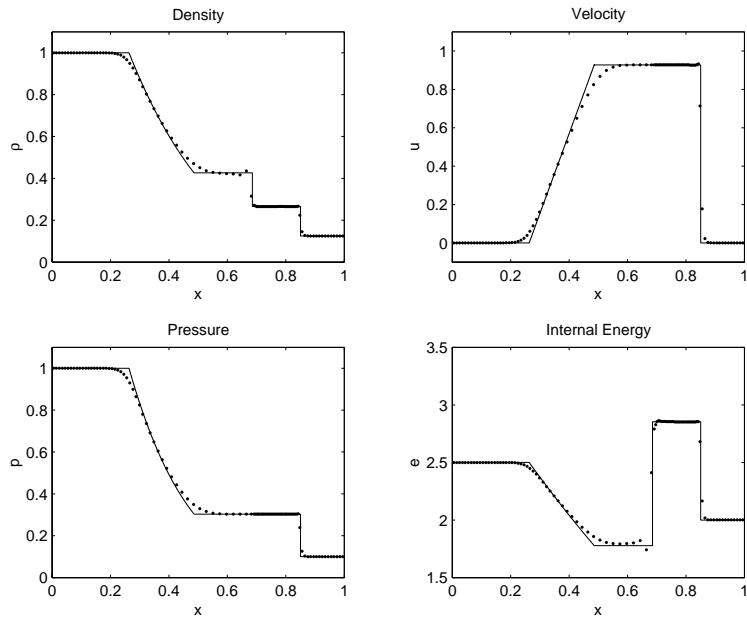


Figure 27: Flux limited version of Roe Lagrange scheme applied to test 1, using the minbee limiter. Numerical (dotted line) and exact (solid line) solutions are evaluated at time 0.2 units.

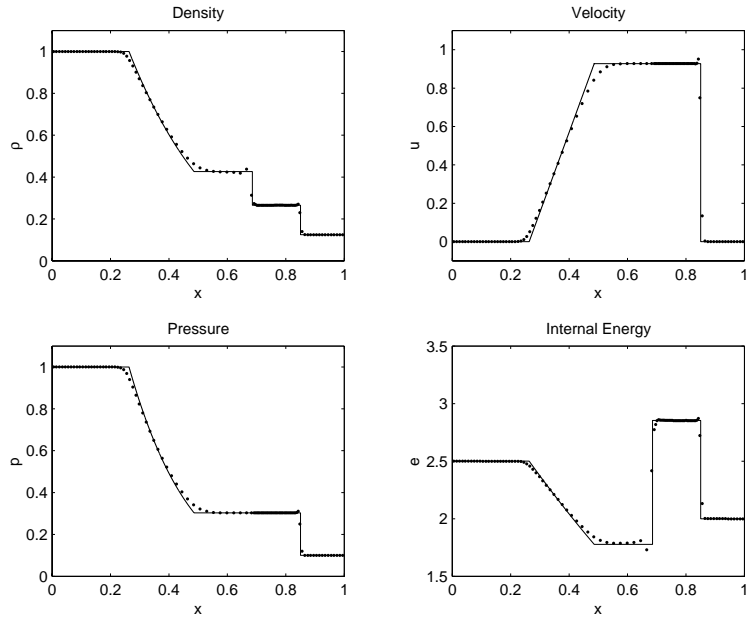


Figure 28: Flux limited version of Roe Lagrange scheme applied to test 1, using the Van Leer limiter. Numerical (dotted line) and exact (solid line) solutions are evaluated at time 0.2 units.

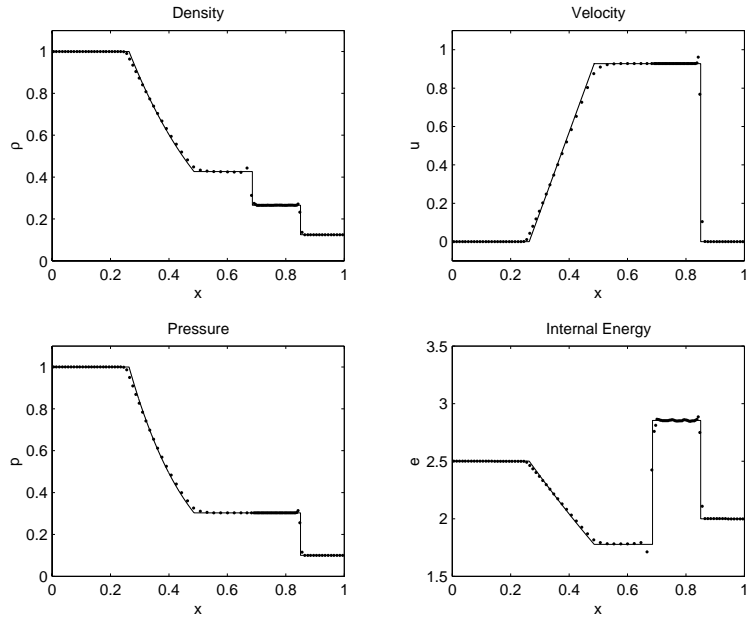


Figure 29: Flux limited version of Roe Lagrange scheme applied to test 1, using the superbee limiter. Numerical (dotted line) and exact (solid line) solutions are evaluated at time 0.2 units.

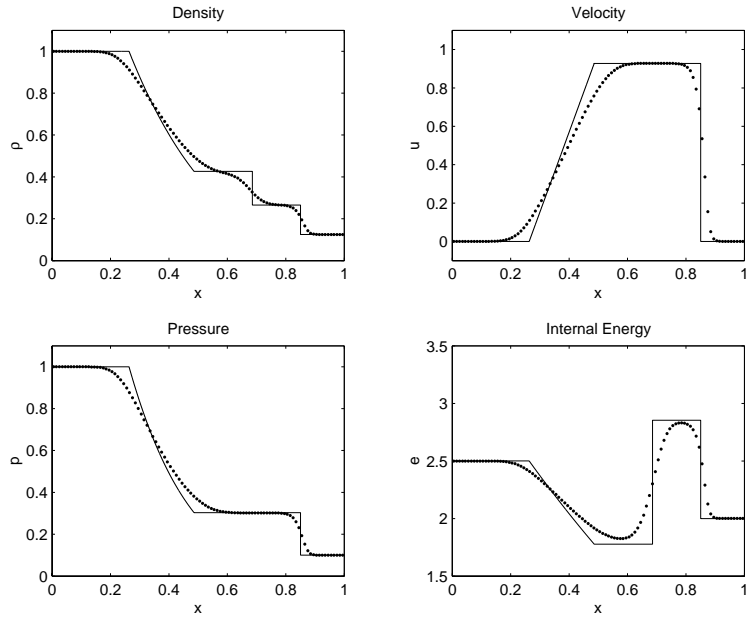


Figure 30: HLLC Lagrangian method applied to test 1, with piecewise constant remap. Numerical (dotted line) and exact (solid line) solutions are evaluated at time 0.2 units.

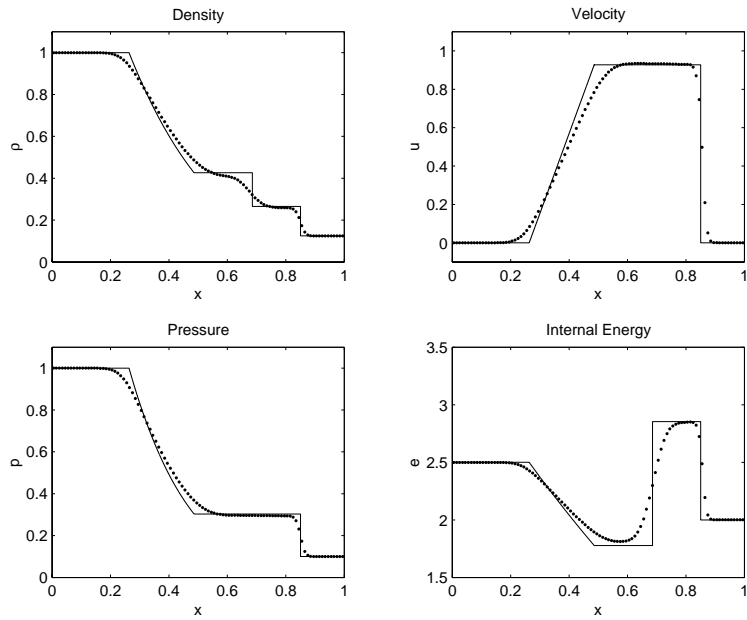


Figure 31: Roe Lagrange method applied to test 1, with piecewise constant remap. Numerical (dotted line) and exact (solid line) solutions are evaluated at time 0.2 units.

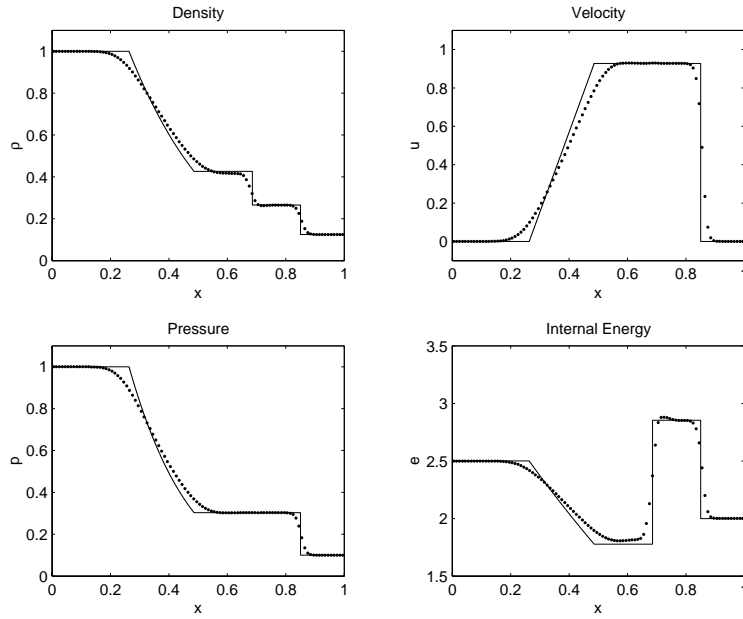


Figure 32: HLLC Lagrangian method applied to test 1, with piecewise linear remap. Numerical (dotted line) and exact (solid line) solutions are evaluated at time 0.2 units.

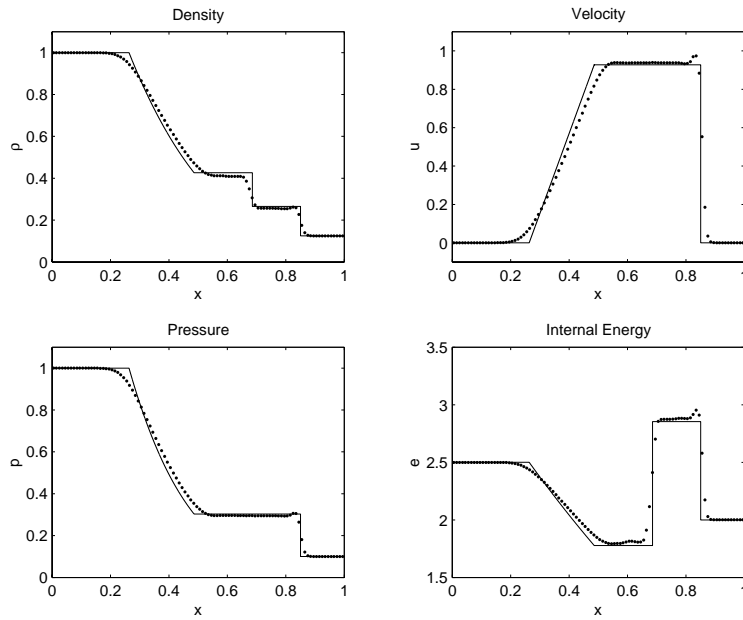


Figure 33: Roe Lagrange method applied to test 1, with piecewise linear remap. Numerical (dotted line) and exact (solid line) solutions are evaluated at time 0.2 units.

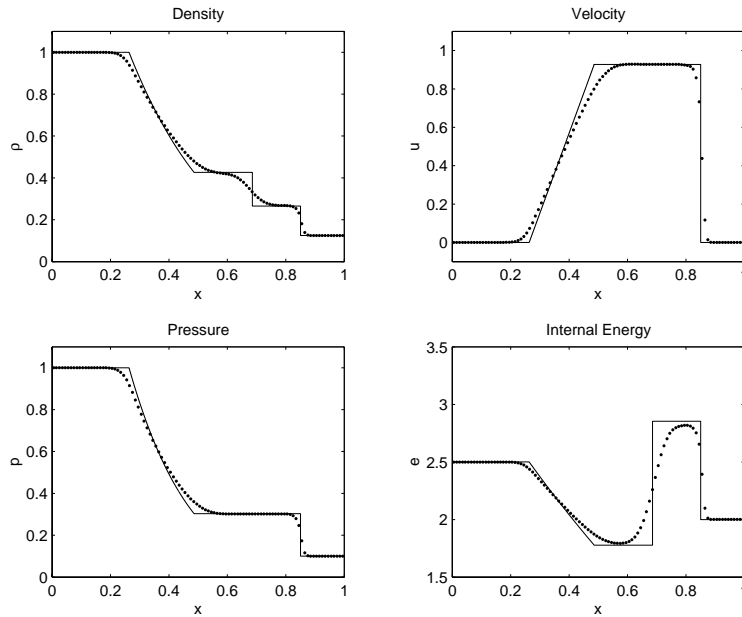


Figure 34: MUSCL-Hancock HLLC Lagrangian method applied to test 1, with conserved variable slope limiting using the minbee limiter, and piecewise constant remap. Numerical (dotted line) and exact (solid line) solutions are evaluated at time 0.2 units.

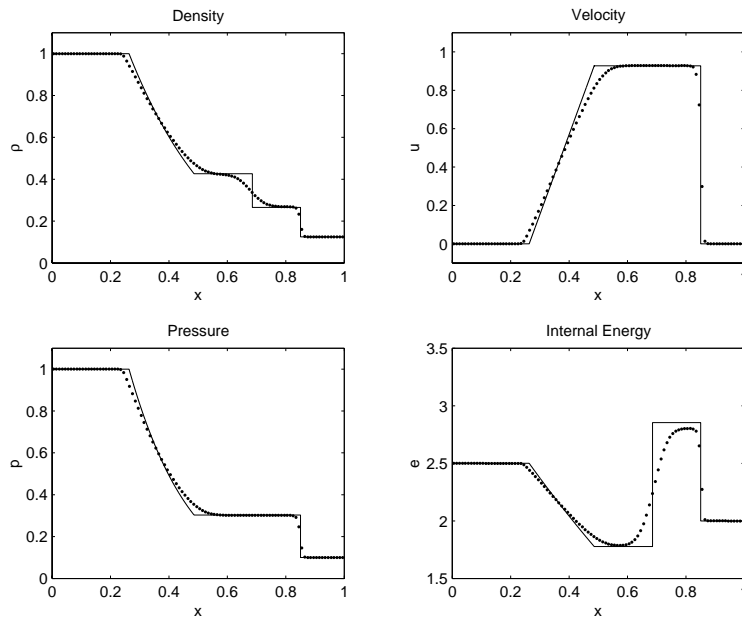


Figure 35: MUSCL-Hancock HLLC Lagrangian method applied to test 1, with conserved variable slope limiting using the superbee limiter, and piecewise constant remap. Numerical (dotted line) and exact (solid line) solutions are evaluated at time 0.2 units.

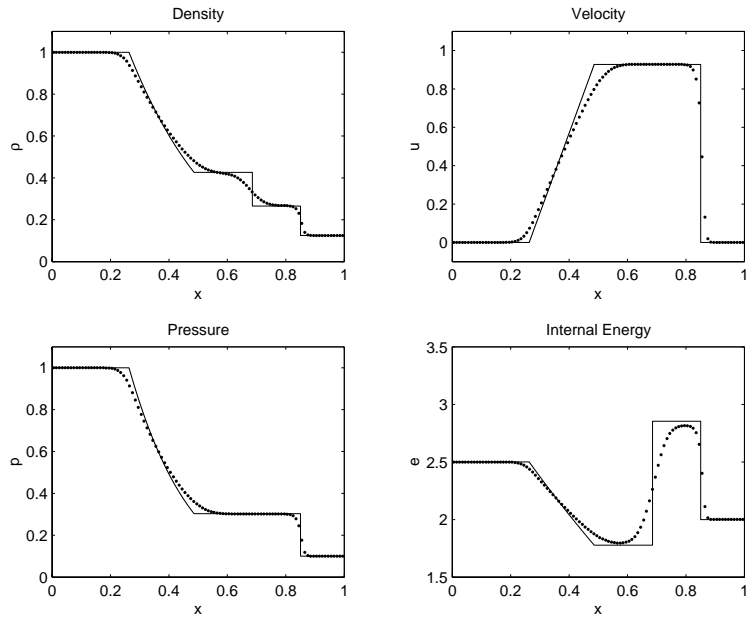


Figure 36: MUSCL-Hancock HLLC Lagrangian method applied to test 1, with wave-by-wave slope limiting using the minbee limiter, and piecewise constant remap. Numerical (dotted line) and exact (solid line) solutions are evaluated at time 0.2 units.

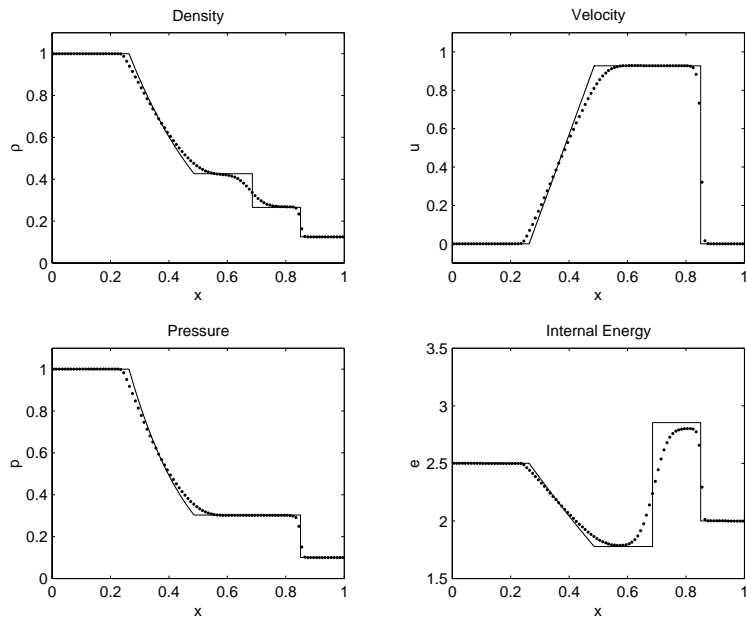


Figure 37: MUSCL-Hancock HLLC Lagrangian method applied to test 1, with wave-by-wave slope limiting using the superbee limiter, and piecewise constant remap. Numerical (dotted line) and exact (solid line) solutions are evaluated at time 0.2 units.

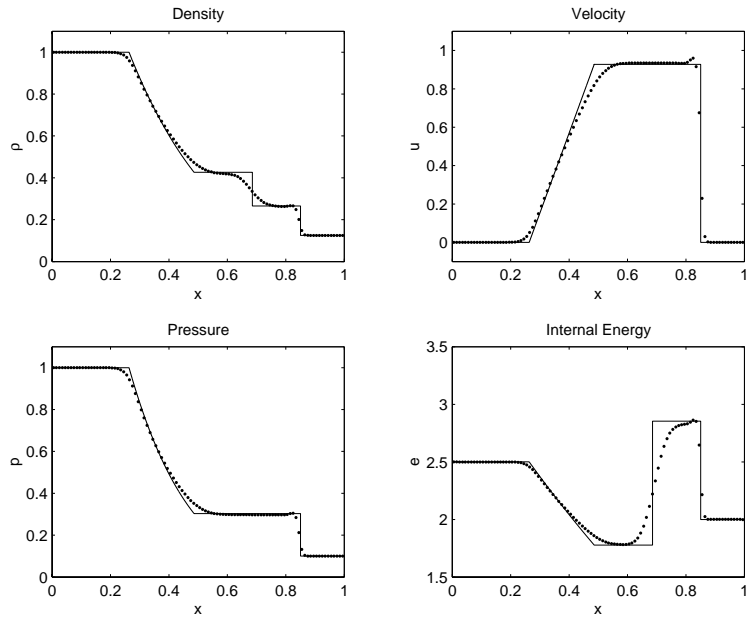


Figure 38: Flux limited version of Roe Lagrange scheme applied to test 1, using the minbee limiter and piecewise constant remap. Numerical (dotted line) and exact (solid line) solutions are evaluated at time 0.2 units.

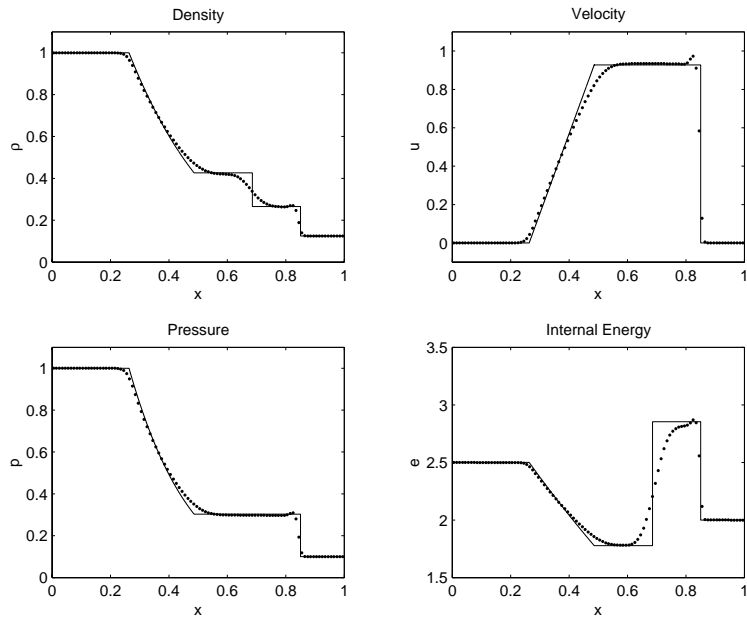


Figure 39: Flux limited version of Roe Lagrange scheme applied to test 1, using the Van Leer limiter and piecewise constant remap. Numerical (dotted line) and exact (solid line) solutions are evaluated at time 0.2 units.

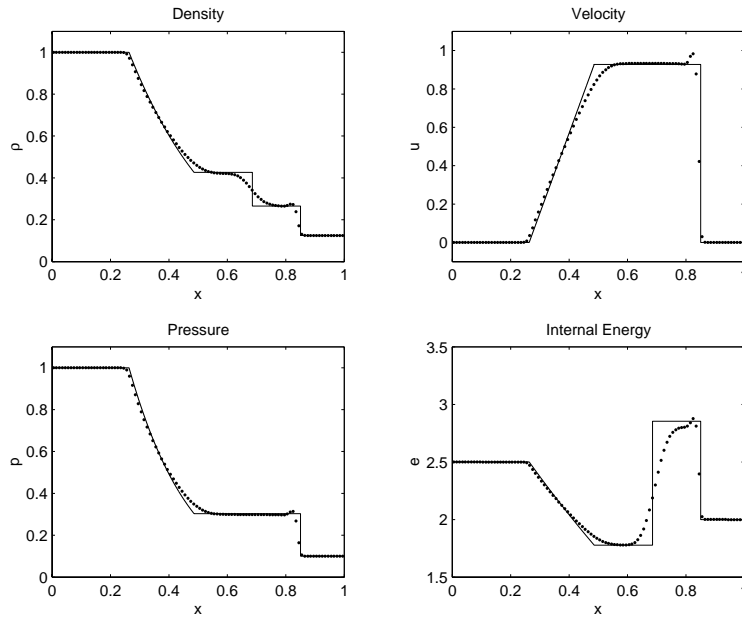


Figure 40: Flux limited version of Roe Lagrange scheme applied to test 1, using the superbee limiter, and piecewise constant remap. Numerical (dotted line) and exact (solid line) solutions are evaluated at time 0.2 units.

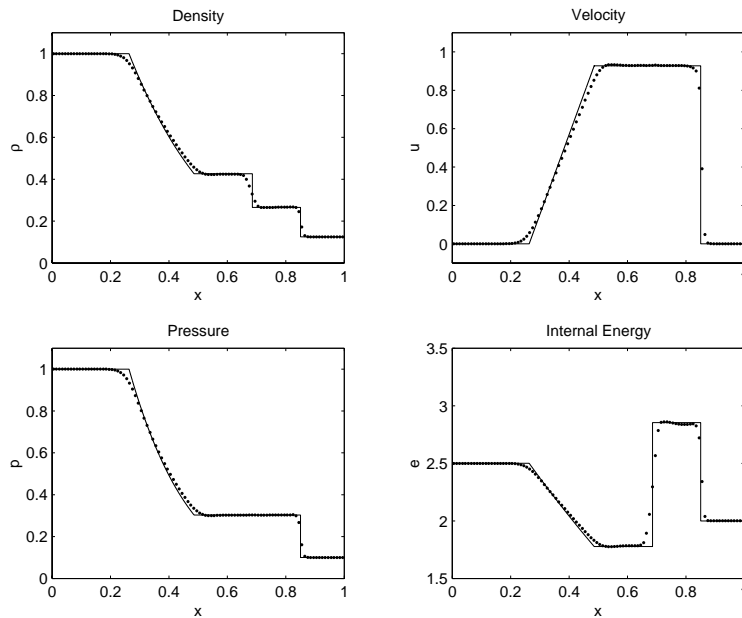


Figure 41: MUSCL-Hancock HLLC Lagrangian method applied to test 1, with conserved variable slope limiting using the minbee limiter, and piecewise linear remap. Numerical (dotted line) and exact (solid line) solutions are evaluated at time 0.2 units.

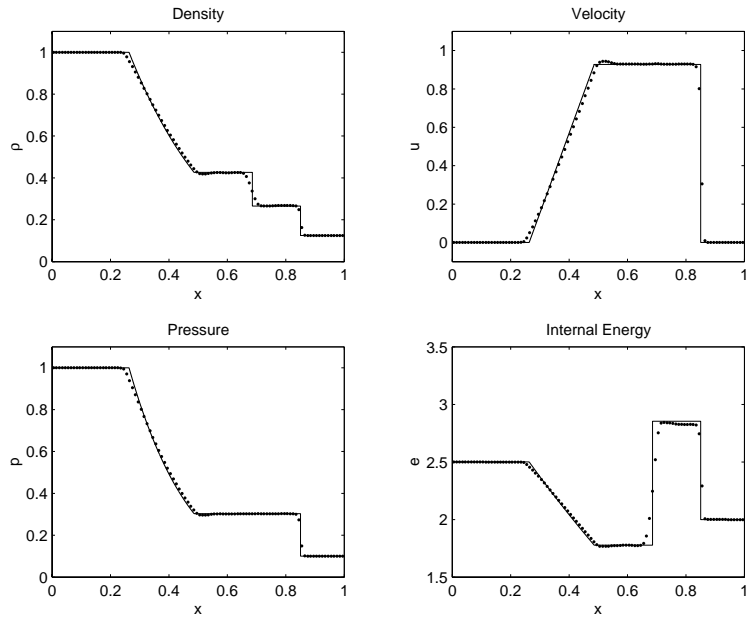


Figure 42: MUSCL-Hancock HLLC Lagrangian method applied to test 1, with conserved variable slope limiting using the superbee limiter, and piecewise linear remap. Numerical (dotted line) and exact (solid line) solutions are evaluated at time 0.2 units

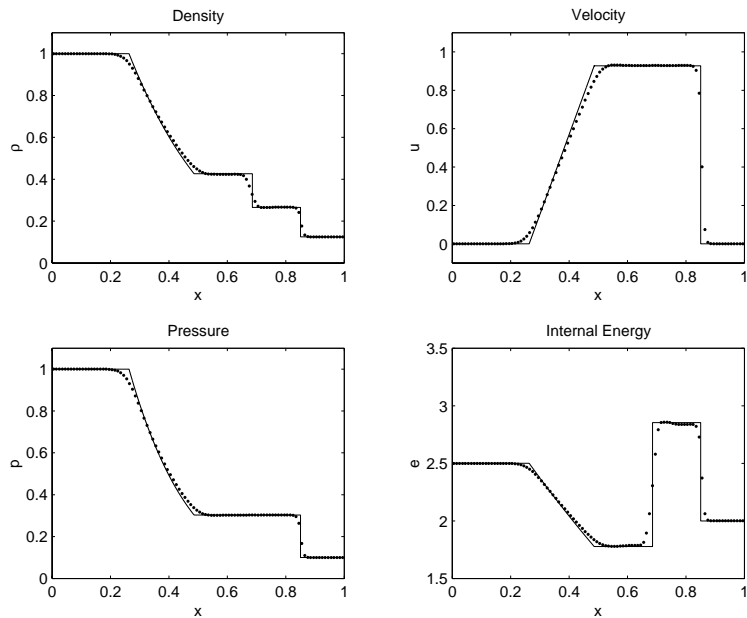


Figure 43: MUSCL-Hancock HLLC Lagrangian method applied to test 1, with wave-by-wave slope limiting using the minbee limiter, and piecewise linear remap. Numerical (dotted line) and exact (solid line) solutions are evaluated at time 0.2 units.

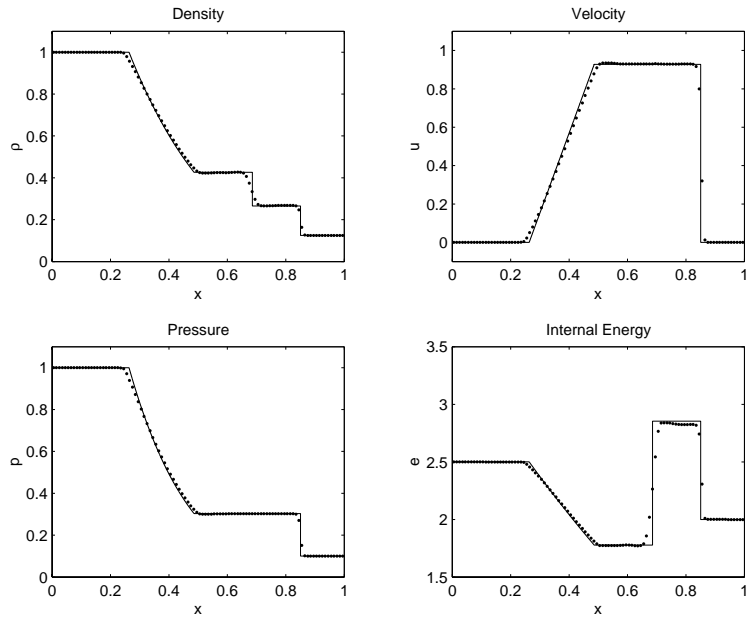


Figure 44: MUSCL-Hancock HLLC Lagrangian method applied to test 1, with wave-by-wave slope limiting using the superbee limiter, and piecewise linear remap. Numerical (dotted line) and exact (solid line) solutions are evaluated at time 0.2 units

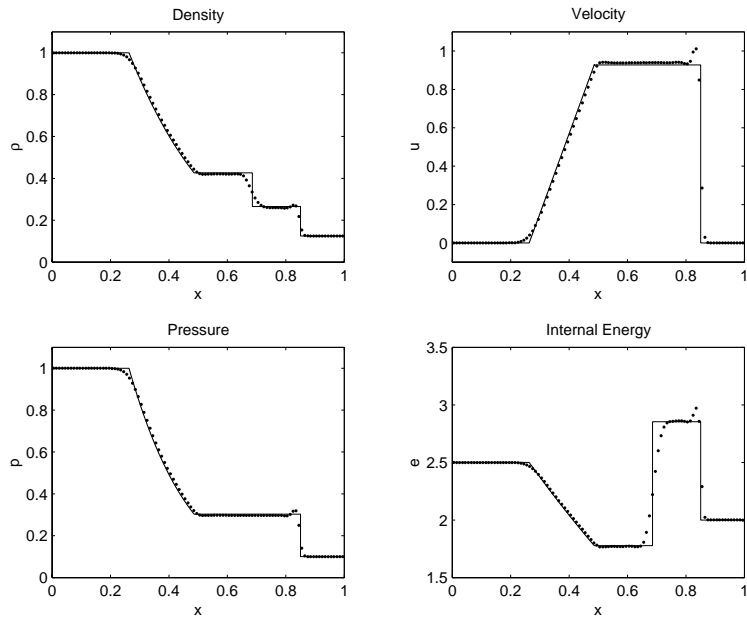


Figure 45: Flux limited version of Roe Lagrange scheme applied to test 1, using the minbee limiter and piecewise linear remap. Numerical (dotted line) and exact (solid line) solutions are evaluated at time 0.2 units.

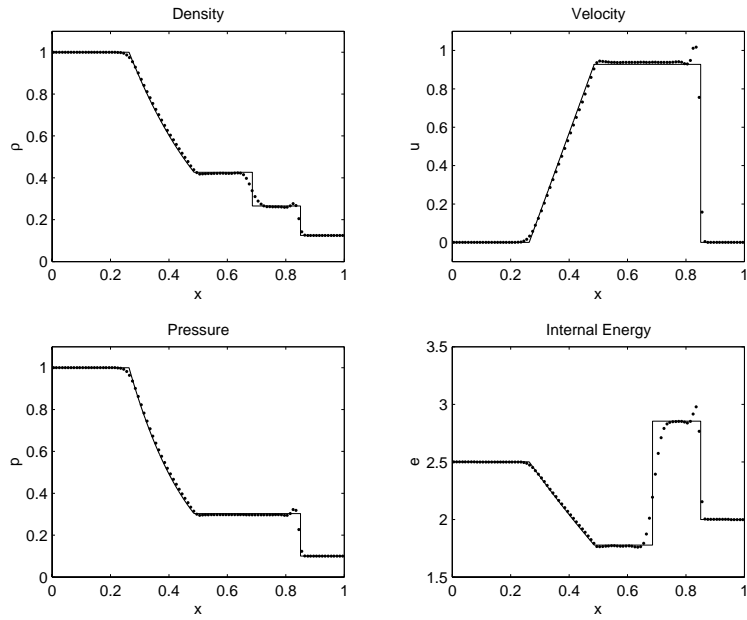


Figure 46: Flux limited version of Roe Lagrange scheme applied to test 1, using the Van Leer limiter and piecewise linear remap. Numerical (dotted line) and exact (solid line) solutions are evaluated at time 0.2 units.

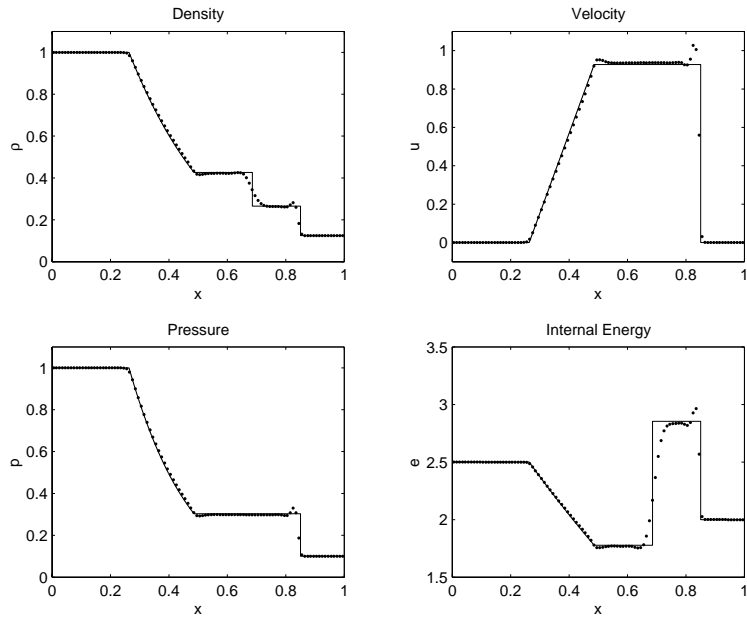


Figure 47: Flux limited version of Roe Lagrange scheme applied to test 1, using the superbee limiter, and piecewise linear remap. Numerical (dotted line) and exact (solid line) solutions are evaluated at time 0.2 units.

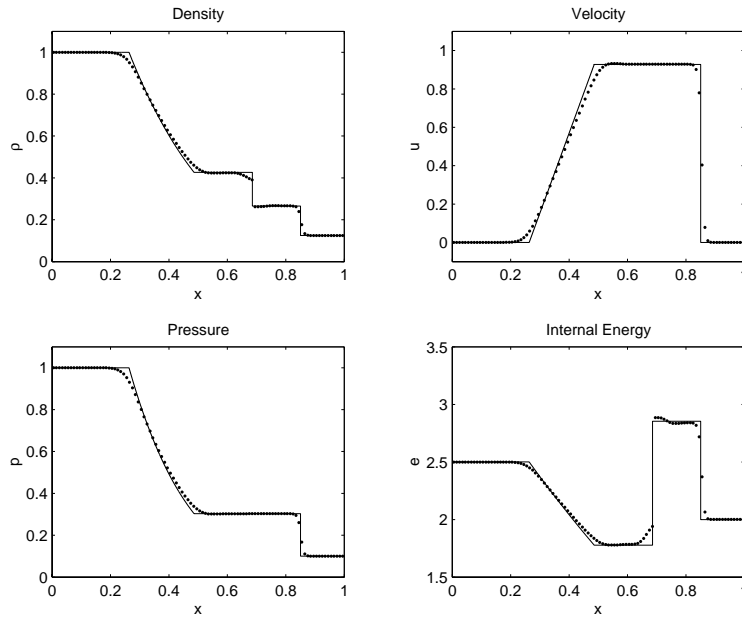


Figure 48: MUSCL-Hancock HLLC Lagrangian method applied to test 1, with wave-by-wave slope limiting using the minbee limiter, and piecewise linear remap. Numerical (dotted line) and exact (solid line) solutions are evaluated at time 0.2 units.

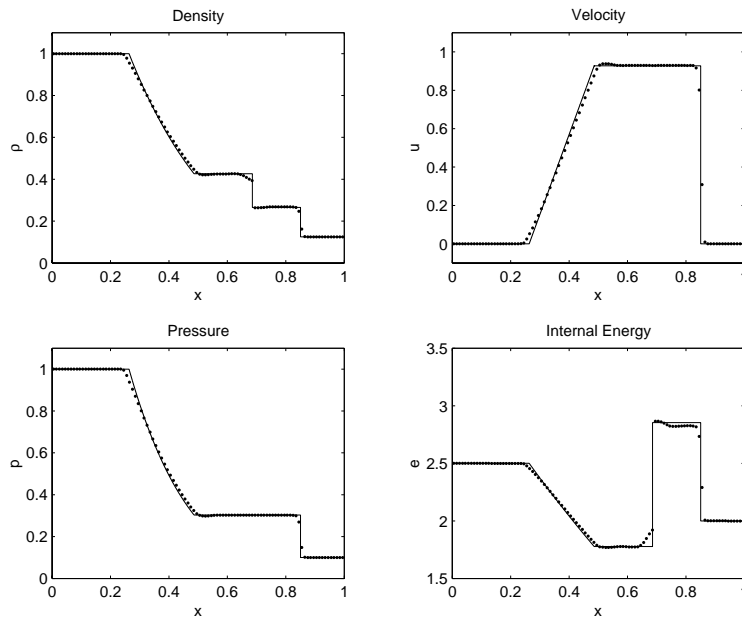


Figure 49: MUSCL-Hancock HLLC Lagrangian method applied to test 1, with wave-by-wave slope limiting using the minbee limiter, and piecewise linear remap. Numerical (dotted line) and exact (solid line) solutions are evaluated at time 0.2 units.

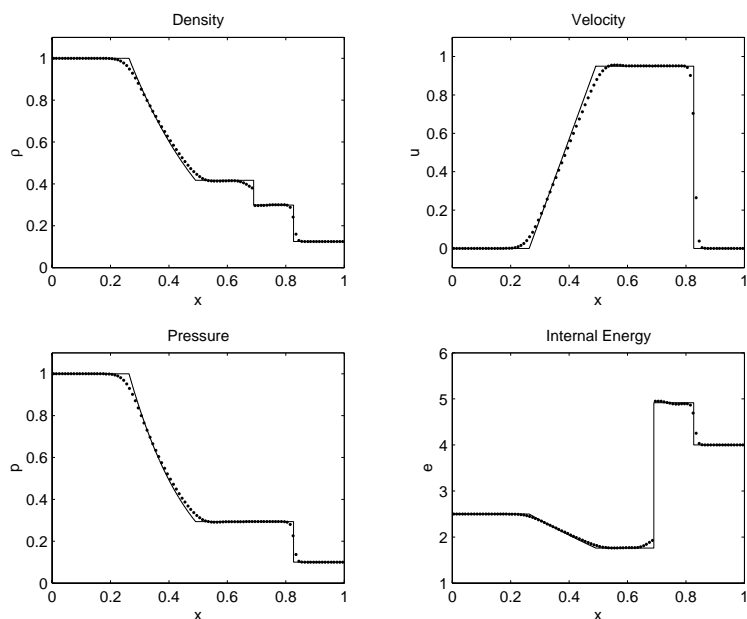


Figure 50: MUSCL-Hancock HLLC Lagrangian method applied to test 2, with wave-by-wave slope limiting using the minbee limiter, and piecewise linear remap. Numerical (dotted line) and exact (solid line) solutions are evaluated at time 0.2 units.

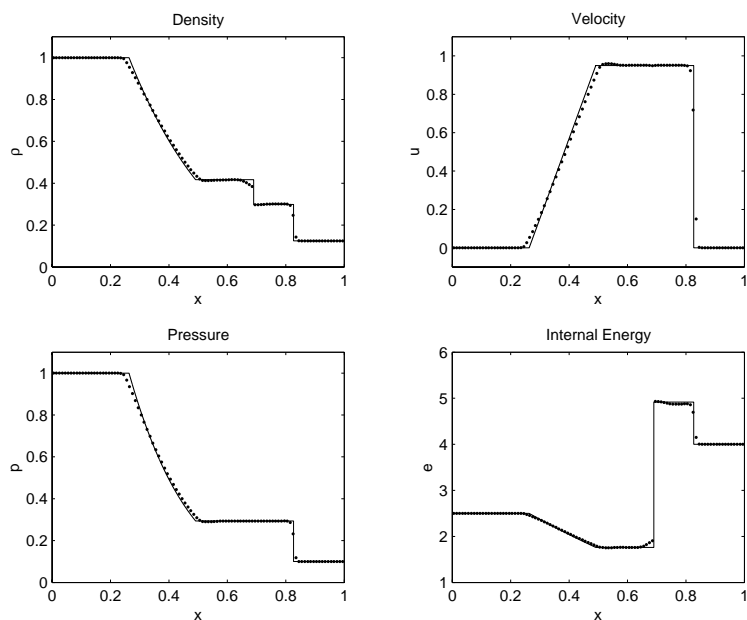


Figure 51: MUSCL-Hancock HLLC Lagrangian method applied to test 2, with wave-by-wave slope limiting using the minbee limiter, and piecewise linear remap. Numerical (dotted line) and exact (solid line) solutions are evaluated at time 0.2 units.

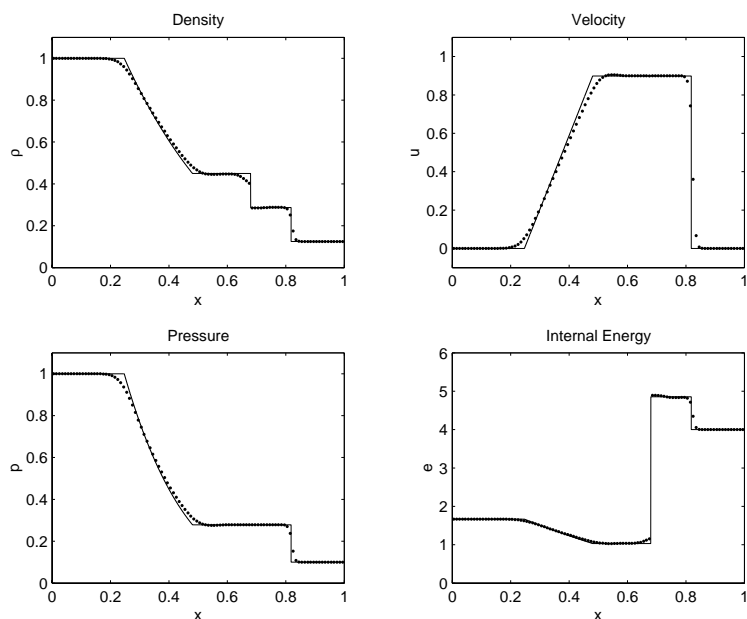


Figure 52: MUSCL-Hancock HLLC Lagrangian method applied to test 3, with wave-by-wave slope limiting using the minbee limiter, and piecewise linear remap. Numerical (dotted line) and exact (solid line) solutions are evaluated at time 0.2 units.

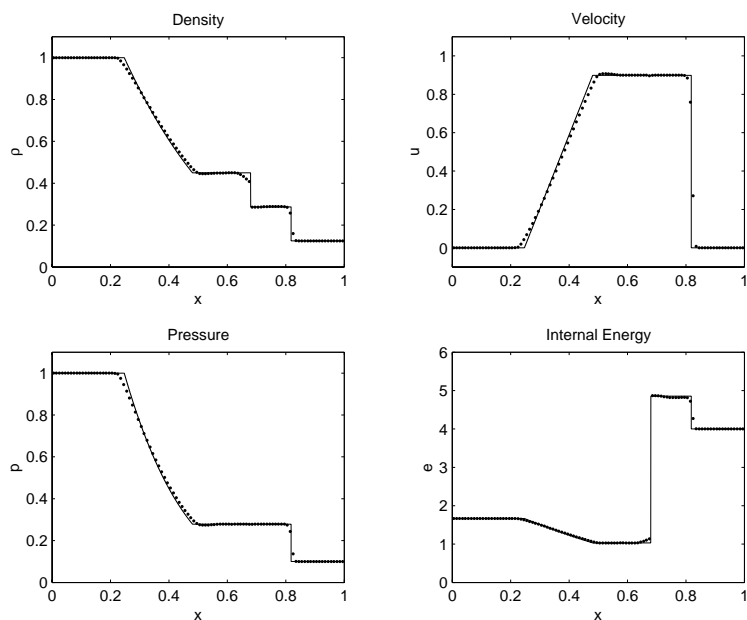


Figure 53: MUSCL-Hancock HLLC Lagrangian method applied to test 3, with wave-by-wave slope limiting using the minbee limiter, and piecewise linear remap. Numerical (dotted line) and exact (solid line) solutions are evaluated at time 0.2 units.

References

- [1] G. Ball. A Free-Lagrange method for unsteady compressible flow: simulation of a confined cylindrical blast wave, *Shock Waves*, 5 (1996), pp. 311-325.
- [2] R. Courant, E. Isaacson, and M. Rees. On the solution of nonlinear hyperbolic differential equation by finite differences, *Comm. Pure. Appl. Math.* 5 (1952) pp. 243-255.
- [3] A. Harten. P. D. Lax, and B. van Leer. On upstream differencing and Godunov-type schemes for hyperbolic conservation laws, *SIAM Review*, 25(1) (1983) pp. 35-61.
- [4] R. J. LeVeque. Numerical methods for conservation laws. Birkhäuser Verlag (1992).
- [5] H. Luo, J. D. Baum and R. Löhner. On the computation of multi-material flows using ALE formulation.
- [6] W. J. Rider. A review of approximate riemann solvers with godunov's method in lagrangian coordinates, Los Alamos National Laboratory (1994).
- [7] P. L. Roe. Approximate Riemann solver, parameter vectors, and difference schemes, *Journal of Computational Physics*, 43 (1981) pp. 357-372.
- [8] P. Sims. Interface tracking using lagrangian-Eulerian methods. PhD Thesis (1990).
- [9] G. Sod. A survey of several finite difference methods for systems of nonlinear hyperbolic conservation laws, *Journal of Computational Physics*, 27 (1978), pp. 1-31.
- [10] S. Stokes. Euler Methods with a lagrangian phase in gas dynamics, Msc dissertation, Reading University (1995).
- [11] J. Y. Treèpanier, M. Reggio, M. Paraschivoiu and R. Camarero. Unsteady Euler solutions for arbitrarily moving bodies and boundaries, *American Institute of Aeronautics and Astronautics*, 31 (1993) pp. 1869-1876.
- [12] E. F. Toro. Riemann solvers and numerical methods for fluid dynamics, Springer-Verlag (1997).

- [13] E. F. Toro, M. Spruce, and W. Speares. Restoration of the contact surface in the HLL-Riemann solver. *Shock Waves*, 4 (1994), pp. 25-34.
- [14] B. van Leer. Towards the ultimate conservative difference scheme IV. A new approach to numerical convection, *Journal of Computational Physics*, 23 (1977) pp. 276-299.
- [15] C. D. Munz. On godunov-type schemes for lagrangian gas dynamics, *SIAM Journal of Numerical Analysis*, 31 (1994) No. 1, pp. 17-42.

List of Figures

1	$x - t$ diagram of the computational mesh	5
2	Schematic of approximate Riemann solution in Lagrangian control volume ABC.	7
3	Wave-by-wave decomposition of gradients obtained from local solutions of Riemann problems, with cell averages as initial data.	13
4	Schematic of approximate Riemann solution in Lagrangian control volume ABC.	15
5	$x - U$ diagrams for cell I_i of non-uniform movement to the left and to the right resulting from the Lagrangian phase.	20
6	$x - U$ diagrams for cell I_i of cell contraction and expansion resulting from the Lagrangian phase.	21
7	$x - U$ diagrams illustrating initial cell merging to the right of the material interface.	24
8	$x - U$ diagrams illustrating initial cell merging to the left of the material interface.	25
9	$x - U$ diagrams illustrating in (a) the Lagrangian phase and in (b) the amended remap procedure at the material interface when $u_{int-\frac{1}{2}} > 0$	26
10	$x - U$ diagram illustrating cell reconstruction for $u_{int-\frac{1}{2}} > 0$	28
11	$x - U$ diagram illustrating cell reconstruction for $u_{int-\frac{1}{2}} < 0$	29
12	HLLC Eulerian method applied to test 1	39
13	Roe Eulerian method applied to test 1	39
14	MUSCL-Hancock HLLC Eulerian method applied to test 1, with conserved variable slope limiting using the minbee limiter	40
15	MUSCL-Hancock HLLC Eulerian method applied to test 1, with conserved variable slope limiting using the superbee limiter	40
16	MUSCL-Hancock HLLC Eulerian method applied to test 1, with wave-by-wave slope limiting using the minbee limiter	41
17	MUSCL-Hancock HLLC Eulerian method applied to test 1, with wave-by-wave slope limiting using the superbee limiter	41
18	Flux limited version of Roe Eulerian method applied to test 1, using the minbee limiter	42
19	Flux limited version of Roe Eulerian method applied to test 1, using the Van Leer limiter	42
20	Flux limited version of Roe Eulerian method applied to test 1, using the superbee limiter	43
21	HLLC Lagrangian method applied to test 1	43
22	Roe Lagrange method applied to test 1	44
23	MUSCL-Hancock HLLC Lagrangian method applied to test 1, with conserved variable slope limiting using the minbee limiter	44

24	MUSCL-Hancock HLLC Lagrangian method applied to test 1, with conserved variable slope limiting using the superbee limiter	45
25	MUSCL-Hancock HLLC Lagrangian method applied to test 1, with wave-by-wave slope limiting using the minbee limiter	45
26	MUSCL-Hancock HLLC Lagrangian method applied to test 1, with wave-by-wave slope limiting using the superbee limiter	46
27	Flux limited version of Roe Lagrange scheme applied to test 1, using the minbee limiter	46
28	Flux limited version of Roe Lagrange scheme applied to test 1, using the Van Leer limiter	47
29	Flux limited version of Roe Lagrange scheme applied to test 1, using the superbee limiter	47
30	HLLC Lagrangian method applied to test 1, with piecewise constant remap	48
31	Roe Lagrange method applied to test 1, with piecewise constant remap	48
32	HLLC Lagrangian method applied to test 1, with piecewise linear remap	49
33	Roe Lagrange method applied to test 1, with piecewise linear remap	49
34	MUSCL-Hancock HLLC Lagrangian method applied to test 1, with conserved variable slope limiting using the minbee limiter, and piecewise constant remap	50
35	MUSCL-Hancock HLLC Lagrangian method applied to test 1, with conserved variable slope limiting using the superbee limiter, and piecewise constant remap	50
36	MUSCL-Hancock HLLC Lagrangian method applied to test 1, with wave-by-wave slope limiting using the minbee limiter, and piecewise constant remap	51
37	MUSCL-Hancock HLLC Lagrangian method applied to test 1, with wave-by-wave slope limiting using the superbee limiter, and piecewise constant remap	51
38	Flux limited version of Roe Lagrange scheme applied to test 1, using the minbee limiter and piecewise constant remap	52
39	Flux limited version of Roe Lagrange scheme applied to test 1, using the Van Leer limiter and piecewise constant remap	52
40	Flux limited version of Roe Lagrange scheme applied to test 1, using the superbee limiter, and piecewise constant remap	53
41	MUSCL-Hancock HLLC Lagrangian method applied to test 1, with conserved variable slope limiting using the minbee limiter, and piecewise linear remap	53

42	MUSCL-Hancock HLLC Lagrangian method applied to test 1, with conserved variable slope limiting using the superbee limiter, and piecewise linear remap	54
43	MUSCL-Hancock HLLC Lagrangian method applied to test 1, with wave-by-wave slope limiting using the minbee limiter, and piecewise linear remap	54
44	MUSCL-Hancock HLLC Lagrangian method applied to test 1, with wave-by-wave slope limiting using the superbee limiter, and piecewise linear remap	55
45	Flux limited version of Roe Lagrange scheme applied to test 1, using the minbee limiter and piecewise linear remap	55
46	Flux limited version of Roe Lagrange scheme applied to test 1, using the Van Leer limiter and piecewise linear remap	56
47	Flux limited version of Roe Lagrange scheme applied to test 1, using the superbee limiter, and piecewise linear remap	56
48	MUSCL-Hancock HLLC Lagrangian method applied to test 1, with wave-by-wave slope limiting using the minbee limiter, and piecewise linear remap.	57
49	MUSCL-Hancock HLLC Lagrangian method applied to test 1, with wave-by-wave slope limiting using the minbee limiter, and piecewise linear remap.	57
50	MUSCL-Hancock HLLC Lagrangian method applied to test 2, with wave-by-wave slope limiting using the minbee limiter, and piecewise linear remap.	58
51	MUSCL-Hancock HLLC Lagrangian method applied to test 2, with wave-by-wave slope limiting using the minbee limiter, and piecewise linear remap.	58
52	MUSCL-Hancock HLLC Lagrangian method applied to test 3, with wave-by-wave slope limiting using the minbee limiter, and piecewise linear remap.	59
53	MUSCL-Hancock HLLC Lagrangian method applied to test 3, with wave-by-wave slope limiting using the minbee limiter, and piecewise linear remap.	59